High-throughput diversification of protein-ligand surfaces to discover chemical inducers of proximity

James B. Shaum[1], Erica A. Steen[1], Miquel Muñoz i Ordoño[2], Daniela V. Wenge[3], Hakyung Cheong[4], Moritz Hunkeler[4,5], Eric M. Bilotta[1], Zoe Rutter[6], Paige A. Barta[1], Natalia Milosevich[1], Lauren M. Hargis[1], Jordan Janowski[1], Timothy R. Bishop[1], Trever R. Carter[1], Bryce da Camara[1], Matthias Hinterndorfer[2], Lucas Dada[7], Wen-Ji He[1], Fabian Offensperger[2], Hirotake Furihata[6], Sydney R. Schweber[3], Charlie Hatton[3], Yanhe (Crane) Wen[3], Benjamin F. Cravatt[1], Keary M. Engle[1], Bruno Melillo[1], Seiya Kitamura[7], Alessio Ciulli[6], Scott A. Armstrong[3], Eric S. Fischer[4,5], Georg E. Winter[2], Michael A. Erb[1*]

[1] Department of Chemistry, The Scripps Research Institute, La Jolla, California, USA.
[2] CeMM Research Center for Molecular Medicine of the Austrian Academy of Sciences, Vienna, Austria.
[3] Division of Hematology/Oncology, Department of Pediatric Oncology, Dana-Farber Cancer Institute, Boston Children's Hospital, and Harvard Medical School, Boston, MA, USA.
[4] Department of Cancer Biology, Dana-Farber Cancer Institute, Boston, MA, USA.
[5] Department of Biological Chemistry and Molecular Pharmacology, Harvard Medical School, Boston, MA, USA
[6] Centre for Targeted Protein Degradation, School of Life Sciences, University of Dundee, Dundee, UK.
[7] Department of Biochemistry, Albert Einstein College of Medicine, Bronx, New York, USA

*Corresponding author. Email: michaelerb@scripps.edu.

Abstract: Chemical inducers of proximity (CIPs) stabilize biomolecular interactions, often causing a privileged rewiring of cellular biochemistry. While rational design strategies can expedite the discovery of heterobifunctional CIPs, molecular glues have predominantly been discovered by serendipity. Envisioning a prospective approach to discover molecular glues for a pre-selected target, we hypothesized that pre-existing ligands could be systematically decorated with chemical modifications to discover protein-ligand surfaces that are tuned to cooperatively engage another protein interface. Using high-throughput chemical synthesis to diversify a ligand for the transcriptional coactivator ENL with 3,163 structurally diverse chemical building blocks, we discovered a compound dHTC1 that elicits potent, selective, and stereochemistry-dependent degradation of ENL by induced binding to $CRL4^{CRBN}$. Unlike prior CRBN-based degraders, dHTC1 binds the ligase with high affinity only after forming the ENL:dHTC1 complex, relying on a hybrid interface of protein-protein and protein-ligand contacts. Altogether, this study points toward an expanded chemical space for co-opting the therapeutically important substrate receptor, CRBN, and a second proof-of-concept extending this approach to BRD4 further validates high-throughput chemistry as a facile tool to discover new degraders.

Introduction:

Chemical inducers of proximity (CIPs) include bifunctional small molecules and molecular glues that induce proximity between two targets, often leading to neomorphic effects that are difficult to achieve with other pharmacological approaches (*1, 2*). The first CIPs were discovered serendipitously by studying the mechanisms of action of natural product immunosuppressants (*3, 4*), whereas later efforts made it possible to design bifunctional compounds that simultaneously bind two proteins to enforce their proximity (*5*). For example, proteolysis targeting chimeras (PROTACs), which induce targeted protein degradation, are designed by connecting two ligands that independently bind to a target of interest and an E3 ubiquitin ligase (*6*). Molecular glues function as CIPs without needing to bind both targets independently, instead forming a composite protein-ligand surface that cooperatively stabilizes an interfacial protein-protein interaction (*7*). Thalidomide analogs (also known as immunomodulator imide drugs, IMiDs) – anti-cancer agents that function through this mechanism – resurface the E3 substrate receptor, CRBN, to induce the ubiquitination and degradation of *neo*-substrate targets, including therapeutically important transcription factors (*8-17*). This highlights the potential for molecular glues to address difficult classes of drug targets, yet prospective approaches to discover molecular glues remain limited.

Lacking modular design principles like those that benefit the discovery of bifunctional CIPs, most molecular glues have been discovered through retrospective mechanism of action studies (*1, 2*). We considered it instructive that several recently discovered molecular glues have close structural analogs that bind the same target but do not function as glues (*18-25*). In these examples, CIP behavior can be attributed to subtle structural differences that project outward toward the solvent, forming a composite protein-ligand surface that can stabilize an interfacial interaction (*19, 20, 25*). However, due to the sporadic and primarily serendipitous nature of these discoveries, we lack an understanding of the frequency with which unbiased structural alterations can confer glue-type activity to a ligand and whether these alterations can be identified prospectively for a pre-selected target of interest. We considered that high-throughput chemical synthesis could be used to systematically diversify the surface topology of a protein-ligand complex at scale. Coupled to a phenotypic readout of neomorphic behavior, such as targeted protein degradation, this would allow for the prospective discovery of structural alterations that convert a ligand into a CIP.

Results:

High-throughput chemical diversification to discover degraders for a pre-selected target

We selected JQ1 (**1**), a potent and selective ligand for the BET family bromodomain proteins (BRD2/3/4) to establish an initial proof-of-concept (*26*). Several JQ1 analogs have been reported to possess molecular glue or monovalent degrader activity (*24, 25, 27-30*), motivating us to hypothesize that novel BRD4 degraders could be discovered prospectively by diversifying a solvent-exposed region of JQ1 into several thousand JQ1 analogs. We tested this using sulfur(VI)-fluoride exchange (SuFEx)-based “click chemistry” transformations, whereby iminosulfur oxydifluoride SuFEx hubs react to completion with primary and secondary aliphatic amines in DMSO:PBS mixtures (*31-33*). These mild, biocompatible reaction conditions allow for crude products to be tested directly in living cells, thus marrying high-throughput chemistry (HTC) with miniaturized cell-based screens (*34, 35*).

JQ1 was first converted to an anilino intermediate via Buchwald–Hartwig amination assisted by a newly reported Pd(COD)(DQ) catalyst (*36*), which was then furnished with an iminosulfur oxydifluoride SuFEx hub facilitated by a silver pentafluorooxosulfate salt (*37*) (**2**, **Fig. S1A**). Sourcing a commercial library of 3,163 structurally diverse amine building blocks for plate-based HTC, we then synthesized more than 3,000 JQ1 analogs in parallel and screened each for the ability to induce BRD4 degradation (**Fig. S1B** and **Table S1**). Crude products were tested in MV4;11 cells bearing a carboxy (C)-terminally tagged BRD4-HiBiT reporter to identify hits, which were then retested in triplicate for confirmation (**Fig. S1C**). To remove false positives, each hit was also counter-screened in triplicate against MV4;11 cells expressing an amino (N)-terminal HiBiT fusion to ENL, as JQ1 does not bind to ENL (**Fig. S1C,D** and **Table S2**). Based on these data, four hits were prioritized for resynthesis and purification, leading to the positive identification of two BRD4 degraders, **3** and **4** (**Fig. S1E,F**).

Both compounds induced time-dependent and dose-responsive loss of BRD4-HiBiT signal (**Fig. S1G,H**), which could be rescued by excess concentrations of JQ1 (**Fig. S1I,J**), indicating an on-target mechanism of action. The effects of **3** and **4** could also be rescued by the neddylation inhibitor, MLN4924, and the proteasome inhibitor, carfilzomib, altogether establishing that they induce proteasome-dependent degradation of BRD4 through the activity of a cullin-RING ligase (CRL) complex (**Fig. S1I,J**). Degradation of wild-type BRD4 was confirmed by mass spectrometry (MS)-based expression proteomics analyses, which further served to demonstrate that **3** and **4** induce selective degradation of BRD4 (**Fig. S1K,L** and **Table S3**). While degradation was not complete (**Fig. S1G,H**), we note that **3** and **4** are each a mixture of several stereoisomers that may compete for target engagement and thus limit the extent of degradation that is possible to achieve. Nevertheless, these studies established an initial proof-of-concept that motivated further study of HTC for the prospective discovery of CIPs.

High-throughput chemical diversification to discover dHTC1

To test whether this approach is extensible to other targets, including those for which molecular glues have not previously been reported, we selected the leukemia target and transcriptional co-activator, ENL. ENL binds to chromatin through its YEATS domain, which interacts with acetylated lysine side chains (*38, 39*). We previously developed an acetyllysine-competitive inhibitor, SR-0813, that binds to the ENL YEATS domain and displaces ENL from chromatin (*35*). Since SR-0813 does not affect ENL stability (**Fig. S2A**), we reasoned that high-throughput diversification of an ENL ligand could be coupled to screens for ENL degradation to identify structural modifications that convert a ligand into a CIP. To test this, we used SuFEx-based high-throughput chemical diversification of TM-7 (**5**), a synthetically simplified analog of SR-0813 (**Fig. 1A** and **S2A-C**). TM-7 was furnished with an iminosulfur oxydifluoride SuFEx hub (**6**) and further diversified with the same 3,163 amine building blocks (**Fig. 1A**). Each crude product was then screened for the ability to induce ENL degradation using MV4;11 cells expressing HiBiT-ENL (**Fig. 1B** and **Table S4**). A total of 93 hits (**Fig. 1B**, z score < -2) were promptly resynthesized, re-tested for ENL-HiBiT degradation, and counter-screened against BRD4-HiBiT to remove false positives, as TM-7 itself does not bind BRD4 (**Fig. 1C** and **S2D**). One hit, the coupling product of a pyrrolidine spirosuccinimide building block (**7**), selectively decreased ENL-HiBiT signal without impacting BRD4-HiBiT (**Fig. 1C,D** and **Table S5**). To enable validation, the racemic amine building block (**7**) was coupled with **6** at milligram scale and purified by column chromatography, yielding **8**, hereafter referred to as *rac*-dHTC1 to signify that the degrader was discovered using HTC (**Fig. 1D**).

Immunoblot analyses showed that *rac*-dHTC1 is active against natively expressed ENL protein in a panel of acute myeloid leukemia (AML) cell lines, confirming that its effects are not an artifact of the HiBiT reporter tag (**Fig. 1E** and **Fig. S3A**). We observed dose-responsive effects in MV4;11 cells and 5 additional AML cell lines expressing ENL-HiBiT, determining half-maximal degradation concentration (DC_{50}) values ranging from 50 nM to 1.85 μM and maximal degradation (D_{max}) ranging from 91% to 58% (**Fig. S3B**). In MV4;11 cells, degradation was observed as soon as 30 minutes after treatment, maximized after 8 hours, and sustained by a single dose for at least 5 days (**Fig. 1F**).

To study the mechanisms underlying the putative degradation of ENL by *rac*-dHTC1, we used chemical rescue experiments. Pre-treatment with a saturating concentration of the ENL/AF9 YEATS ligand, SR-0813, prevented loss of HiBiT-ENL signal induced by *rac*-dHTC1 treatment (**Fig. 1G**), which established that on-target engagement of ENL was necessary for its activity. Loss of HiBiT-ENL signal could also be rescued by the neddylation inhibitor, MLN4924, and the proteasome inhibitor, carfilzomib (**Fig. 1G**), demonstrating that *rac*-dHTC1 prompts proteasome-dependent degradation of ENL through a CRL.

Finally, we used an expression proteomics analysis to evaluate the selectivity of *rac*-dHTC1 in MV4;11 cells, finding that it degraded ENL exclusively (**Fig. 1H** and **Table S6**). It also selectively decreased the production of proteins encoded by ENL target genes (e.g. HOXA10 and MYC), a known transcriptional consequence of selective ENL degradation in MV4;11 cells (*35*). AF9, a paralog of ENL that is also bound by this chemical series, was too lowly expressed in MV4;11 cells to evaluate degradation by proteomics, but an immunoblot analysis of exogenously expressed AF9 suggests it can also be degraded by dHTC1 (**Fig. S3C**).

ENL degradation proceeds through $CRL4^{CRBN}$

We next used a forward genetic screen to identify potential effectors responsible for dHTC1 activity. This was enabled by a dual fluorescence ENL stability reporter (ENL-TagBFP-P2A-mCherry) expressed in KBM7 cells harboring a doxycycline-inducible Cas9 expression cassette (**Fig. S3D**) – a system we have used previously to characterize molecular glue and bifunctional degraders (*29, 40, 41*). A UPS-focused library of single guide RNAs (sgRNAs) was screened in these cells for the ability to modify the KBM7 response to *rac*-dHTC1 or SR-1114, a CRBN-based ENL/AF9 PROTAC that we previously disclosed (*35*) (**Fig. 2A**). As expected, sgRNAs targeting CRBN had the most substantial effect on the ability of SR-1114 to degrade ENL, along with other subunits of the $CRL4^{CRBN}$ complex, the proteasome, and the COP9 signalosome – altogether consistent with the known mechanisms of CRBN-based PROTACs (*42*). Strikingly, the same machinery was identified in cells treated with *rac*-dHTC1, with CRBN again being the most substantially enriched hit (**Fig. 2A**).

Using CRISPR/Cas9-based gene disruption to engineer CRBN-deficient MV4;11 cells, we confirmed that CRBN is required for degradation of ENL in MV4;11 cells treated with *rac*-dHTC1 (**Fig. 2B** and **S4A**). Furthermore, a saturating concentration of pomalidomide rescued ENL degradation (**Fig. 2C** and **S4B**), pointing toward a mechanism whereby *rac*-dHTC1 contacts the IMiD-binding site of CRBN. This would presumably rely on its spirosuccinimide moiety, which bears resemblance to both the glutarimide motif present in thalidomide analogs and the asparagine cyclic imide modification proposed to be a natural degron recognized CRBN (*43-45*). Consistent with *rac*-dHTC1 functioning through CRBN, we could also demonstrate interactions between ENL and CRBN-DDB1 by surface plasmon resonance (SPR) in the presence of the compound but not in its absence (**Fig. 2D**).

dHTC1 engagement of CRBN is dependent on it first binding ENL

After determining that $CRL4^{CRBN}$ is required for *rac*-dHTC1 activity, several observations indicated that it does not function like a traditional CRBN-based molecular glue or PROTAC. First, we sought to measure CRBN engagement in cells through the rescue of dBET6-induced degradation of BRD4, which proceeds through CRBN (*46*). As expected, previously described CRBN-based molecular glues and PROTACs demonstrated complete rescue of BRD4-HiBiT degradation by saturating the IMiD-binding site of CRBN in MV4;11 cells (**Fig. 2E**). In contrast, *rac*-dHTC1 was surprisingly unable to rescue BRD4 degradation by dBET6 (**Fig. 2E**), indicating that it could not stoichiometrically engage the IMiD-binding site of CRBN in living cells. We confirmed the lack of CRBN affinity *in vitro* by an SPR analysis of ligand binding to the recently disclosed $CRBN^{midi}$ (*47*) construct, which showed weak and non-specific (i.e., unsaturable) binding by dHTC1 and a calculated K_D of close to 50 μM (**Fig. 2F,G**). To further assess target engagement *in vitro*, we used a competitive fluorescence polarization (FP) assay that reports on the displacement of pomalidomide-BODIPY from purified preparations of recombinant CRBN-DDB1 (*14*). Unlike thalidomide, which showed sub-micromolar potency in dose-response assays, we did not detect inhibition by *rac*-dHTC1 until it reached a concentration of 50 μM (**Fig. 2H** and **Table S7**). Even at this high concentration, which is orders of magnitude above its cellular DC_{50}, we did not observe complete inhibition in the assay (**Fig. 2H**). Likewise, the spirosuccinimide building block **7** that was used to discover dHTC1 showed no inhibition of the CRBN FP assay, even at 50 μM (**Fig. 2H**). These data indicated that dHTC1, unlike other CRBN-based degraders, does not independently possess high affinity for CRBN.

Based on these data, we hypothesized that *rac*-dHTC1 might require a pre-formed complex with ENL to engage the IMiD-binding site with high affinity. Indeed, addition of purified recombinant ENL YEATS domain to the FP assay resulted in potent inhibition by *rac*-dHTC1 but did not impact the behavior of thalidomide or the spirosuccinimide building block (**Fig. 2H**). The IC_{50} of *rac*-dHTC1 was shifted from 66 μM to 860 nM by ENL, resulting in a calculated cooperativity α-factor of ~80 (*48*). By comparison, the thalidomide-based ENL PROTAC, SR-1114, also showed a shift in the presence of ENL YEATS, but the cooperativity was substantially lower (α = 3.3) and it potently inhibited FP signal in both the presence and absence of ENL YEATS (**Fig. 2H**). In fact, without the addition of ENL YEATS, the activity of SR-1114 (IC_{50} = 120 nM) closely matched its parent ligand, thalidomide (IC_{50} = 180 nM), highlighting the difference between dHTC1 a traditional CRBN-based PROTAC.

To evaluate the mechanism of CRBN engagement further, we pursued a limited exploration of dHTC1 structure-activity relationship (SAR) by replacing the sulfamide connection with amide (*rac*-**9**) or urea (*rac*-**10**) isosteres (**Fig. S5A**). Compared to *rac*-dHTC1, these analogs showed relatively similar binding to ENL *in vitro* and in cells (**Fig. S5B,C**), but neither could provoke ENL degradation, even at concentrations as high as 50 μM (**Fig. S5D**).

Both analogs showed weak inhibition of the CRBN FP assay in the absence of ENL, comparable to dHTC1 (**Fig. S5E,F**). However, their binding to CRBN was not improved by the addition of ENL YEATS (**Fig. S5E,F**), indicating that the activity of *rac*-dHTC1 is dependent on its ability to cooperatively bind CRBN in the presence of ENL.

Stereoselective and ENL-dependent binding of (S)-dHTC1 to CRBN

To further evaluate dHTC1 SAR, we separated the two enantiomers by preparative supercritical fluid chromatography (SFC) and assigned absolute stereochemical configurations using vibrational circular dichroism (VCD) (**Fig. 3A,B** and **Supplementary Methods S1**). Whereas (*S*)-dHTC1 (**11**) was able to elicit ENL degradation in a time-dependent and dose-responsive manner (DC_{50} = 26 nM at 8 h in MV4;11 cells), (*R*)-dHTC1 (**12**) was completely inactive (**Fig. 3C,D** and **S6A,B**). Both enantiomers bound to ENL identically *in vitro* (K_D = 69-73 nM) and in cells (EC_{50} = 8 μM), and neither enantiomer could produce a detectable level of CRBN engagement in cells (**Fig. S6C-E**). Consistent with the *rac*-dHTC1 results, we observed a weak IC_{50} of 12 μM for (*S*)-dHTC1 in CRBN FP assays, but this was shifted to 93 nM in the presence of ENL YEATS (α = 130, **Fig. 3E**). In contrast, (*R*)-dHTC1 was inactive up to 50 μM in both the presence and absence of ENL YEATS (**Fig. 3F**). Using SPR, we observed interactions between ENL and CRBN-DDB1 in the presence of (*S*)-dHTC1, but not in the presence of its enantiomer (**Fig. 3G**). Therefore, although neither dHTC1 or ENL possess substantial independent affinity for CRBN, the pre-formed ENL:(*S*)-dHTC1 complex can bind with high affinity and cooperativity to induce stereochemistry-dependent ENL degradation. In contrast to the substantial cooperativity observed for dHTC1 binding to CRBN in the presence of ENL, we measured minimal change of dHTC1 binding to the ENL YEATS domain in the presence of CRBN (**Fig. S6F**), potentially explaining the hook effect we observed *in vitro* at high concentrations of the compound (**Fig. 3H**). Notably, we observe no hook effect in degradation assays in cells (**Fig. 3C** and **Fig. S6A**).

Genetic determinants of CRBN-dependent dHTC1 activity

In contrast to previously reported CRBN-based molecular glues and PROTACs, which possess high intrinsic affinity for the ligase, the ENL-dependent binding of dHTC1 suggests a distinct mechanism for coopting CRBN. To further characterize this mechanism, we coupled deep mutational scanning (DMS) of *CRBN* to a fluorescence activated cell sorting (FACS)-based assessment of ENL degradation in the presence of *rac*-dHTC1 or the ENL PROTAC, SR-1114. This was performed with a CRBN-deficient MV4;11 cell line expressing an ENL-BFP-P2A-mCherry construct (**Fig. S7A**), which can mediate ENL degradation upon reintroduction of wild-type CRBN, but not an inactive CRBN-W380I mutant (**Fig. S7B,C**). Using our previously described DMS library that covers all possible point mutations within 10 Å of the IMiD-binding site of CRBN (*49*) (**Fig. S7D**), we found that, overall, the activity of *rac*-dHTC1 was sensitive to many of the same mutations as SR-1114 (**Fig. S8A,B** and **Table S8, S9**), providing a genetic validation that dHTC1 functions through the IMiD-binding site. Furthermore, several mutations were suggested by the screen to preferentially confer resistance to either *rac*-dHTC1 or SR-1114 (**Fig. 4A**). These included P54, G61, W386, V388, W400 and G416 mutations that disfavored the activity of dHTC1 and F102, E147, D149, P352, and H378 mutations that disfavored SR-1114. The selective effects of these mutations were confirmed by both immunoblot and flow cytometry after expressing each candidate mutation individually (rather than in the pooled format of the screen), altogether validating the results of the screen (**Fig. 4B** and **Fig. S8C,D**).

To better inform how these mutations might impact dHTC1 activity selectively, we determined the co-crystal structure of (*S*)-dHTC1 bound to CRBN at a resolution of 2.2 Å using $CRBN^{midi}$ (**Fig. S9A**) (*47, 50*). This showed (*S*)-dHTC1 occupying the IMiD-binding site of CRBN, positioning its spirosuccinimide moiety within the tri-Trp cage formed by W380, W386, and W400 (**Fig. S9B**). The succinimide of dHTC1 makes hydrogen-bonding interactions with the side chain of H378, backbone carbonyl of H378, and backbone nitrogen of W380, which are all similar to the contacts made by the glutarimide of lenalidomide (*51*). However, apart from the sulfamide making hydrogen-bond contacts with the side chains of N351 and W400, the remainder of dHTC1, which is responsible for binding ENL, makes minimal contacts with CRBN.

Focusing on mutant alleles that selectively affected the activity of dHTC1 or SR-1114, we found that these residues generally mapped to distinct hemispheres of the IMiD-binding site (**Fig. S9B**). On one side, W386Y and W400F mutations, which are located within the tri-Trp pocket, as well as an adjacent V388E mutation, all

prevented degradation by dHTC1 without affecting SR-1114 (**Fig. 4B** and **Fig. S9B**). On the other side of the IMiD-binding site, the side chains of P352 and H378 were particularly important for SR-1114 activity (**Fig. S8A-D** and **S9B**). Nearly any mutation of P352, and many of H378, affected SR-1114 activity, whereas none affected dHTC1 (**Fig. S8A-D**). Since these residues are buried within the IMiD-binding site, we hypothesized that they might reflect differences in the binding mode of the dHTC1 spirosuccinimide compared to traditional glutarimide-based CRBN ligands. To evaluate this, we compared our DMS results to a previously published screen of CC-885, a thalidomide analog that suppresses cell growth by inducing CRBN-based degradation of GSPT1 (**Fig. S10A**) (*13, 49*). This comparison indicated that the W386Y mutation, which impacts the activity of dHTC1, but not SR-1114, also does not impact CC-885 activity (**Fig. S10A**), which we confirmed using FACS-based stability reporters for ENL and GSPT1 (**Fig. S10B**). Likewise, several of the P352 mutations that affected the activity of SR-1114, but not dHTC1, also affected CC-885 (**Fig. S10A,B**). Altogether, these data point toward differences in the mode of CRBN engagement by the spirosuccinimide moiety of dHTC1 compared to PROTACs and molecular glues based on glutarimide-based thalidomide analogs.

We also identified compound-selective mutations mapping to regions outside of the IMiD-binding site, which we considered might reflect regions of direct protein-protein contacts between ENL and CRBN. For example, P54 and G61 mutations, which affect dHTC1 more broadly than SR-1114 (**Fig. S8A,B**), are located far from the IMiD-binding site on another face of CRBN (**Fig. S11A**). Another, H353, which is adjacent to the IMiD-binding site but presents outward into the solvent (**Fig. S11B**), showed varying behavior, with some mutations impairing dHTC1 but not SR-1114 or CC-885 and others affecting SR-1114 and CC-885 but not dHTC1 (**Fig. 4A,B; S8A-D; and S10A,B**).

Broad interfacial contacts are made between CRBN and dHTC1-bound ENL

To understand how dHTC1, when bound to ENL YEATS, recruits CRBN, we determined a ternary complex structure of DDB1$^{\Delta BPB}$•CRBN•dHTC-1•ENL YEATS by cryo-electron microscopy (cryo-EM) refined to a global resolution of 2.6 Å (**Table S10**). We additionally obtained a locally refined map focusing on CRBN•dHTC-1•ENL YEATS at a resolution of 2.9 Å (**Fig. 4C,D** and **Fig. S12**). Our model revealed an extensive interfacial interaction between CRBN and ENL YEATS, with a buried solvent-accessible surface area of ~2,258 Å^2 and a high degree of shape complementarity (score of 0.64 on a scale of 0 to 1, with 1 being perfectly complementary) (*52*). This extended interface of complementary protein-protein contacts is in line with the substantial cooperativity we observed for (*S*)-dHTC1 binding to CRBN in the presence of ENL (α = 130, **Fig. 3E**).

The observed interactions are spread widely across the CRBN–ENL YEATS binding interface (**Fig. 4E**). H353 in CRBN is positioned to make interactions with several ENL YEATS residues, notably forming a hydrogen bond with ENL YEATS E74, where we could see connected density in the EM map (**Fig. 4F**). The ENL YEATS R16 side chain is surrounded by several CRBN residues (F102, F150, I152, H353) and stacks between CRBN residues F102 and F150, whose relative positions suggest formation of a cation-π interaction (**Fig. 4G**). We also observed cation-π interactions between CRBN Y355 and ENL YEATS K72 (**Fig. 4H**) and polar-polar interactions between CRBN Q178 and ENL YEATS Q41 (**Fig. 4I**). Compared to known structures of complexes formed by CRBN-based molecular glues, which mostly rely on interactions with the C-terminal domain of CRBN (*14, 15, 53*), the dHTC1-induced complex relies mainly on interactions between the N-terminal domain of CRBN (F102, F150, Q178) and ENL. Collectively, this high-resolution structure revealed that ternary complex formation is facilitated by an unusually extensive protein-protein interface with substantial shape complementarity and further elucidated the distinct mechanism by which dHTC1 induces ENL proximity to CRBN compared to PROTACs and CRBN-based molecular glues.

Stereoselective degradation of ENL in vivo

Finally, we evaluated whether high-throughput ligand diversification afforded a compound with suitable properties for use in translational model systems. These studies were focused on acute myeloid leukemia, as we and others have previously nominated ENL as a potential target for acute leukemia therapeutics (*35, 38, 39*). In cell culture, we found that (*S*)-dHTC1 potently and stereoselectively suppressed the growth of MV4;11 cells but did not impact HL60 cells (**Fig. 5A** and **Fig. S13A**), consistent with the known sensitivities of each cell line to *ENL* loss-of-function (*38, 39*). Importantly, (*R*)-dHTC1 did not impact either cell line, indicating that the anti-proliferative effects

of (*S*)-dHTC1 occur by on-target degradation of ENL through CRBN (**Fig. 5A** and **Fig. S13A**). Next, we determined the pharmacokinetic behavior of *rac*-dHTC1 and the active enantiomer, finding that both showed highly favorable profiles for *in vivo* experimentation (**Fig. S13B,C**). After delivery by intraperitoneal injection, a single 50 mg/kg dose of (*S*)-dHTC1 produced a maximal plasma concentration of nearly 50 μM within 20 min, or 2.5 μM after adjusting for plasma protein binding (**Fig. 5B**). With dHTC1 exposure *in vivo* greatly exceeding its DC_{50} value of ENL degradation *in vitro*, we next evaluated its pharmacodynamic activity using MV4;11 cells for an orthotopic xenotransplantation model of AML. Based on past observations in MV4;11 cells, which showed that ENL levels recover within 24 h after washout of an ENL PROTAC *in vitro* (*35*), we administered (*R*)- or (*S*)-dHTC1 (50 mg/kg) every 12 h and then evaluated ENL degradation 1 h after the third treatment (**Fig. 5C**). This produced a clear, stereoselective degradation of ENL *in vivo*, resulting in a similarly stereoselective effect on gene transcription in transplanted MV4;11 cells (**Fig. 5D,E**). Using a list of ENL target genes in MV4;11 cells previously defined by the binding of ENL to gene promoters (as determined by chromatin immunoprecipitation) (*38*), we found that (*S*)-dHTC1 preferentially represses ENL-dependent gene expression (**Fig. 5F**). We reached the same conclusion using a list of ENL target genes defined by their previously reported responsiveness to ENL degradation via the dTAG system (i.e. dTAG-13-induced degradation of an ENL-FKBP12-F36V fusion) (*38*) (**Fig. 5F**). The active enantiomer of dHTC1 also stereoselectively produced a phenotypic response, increasing the cell surface expression of CD11b in the spleen and peripheral blood (**Fig. 5G**), which is consistent with the pro-differentiation effects of ENL inhibitors and degraders on leukemia cells (*38*). Altogether, these data demonstrate that high-throughput chemical diversification can deliver CIPs with favorable properties for use *in vitro* and *in vivo*.

Discussion:

The efforts that led to the discovery of dHTC1 were motivated by a general lack of target-centric approaches to discover molecular glues. Satisfied that ligand-binding can, in rare instances, create surface alterations that stabilize a defined protein-protein interaction, we sought a method to alter protein-ligand surfaces systematically and at scale for a pre-defined target of interest. We hypothesized that such a method could enable the prospective discovery of rare protein-ligand hybrid interfaces that are tuned to form cooperative protein-protein interactions, using targeted protein degradation for proof of concept. This was principally inspired by the report of BCL6 and CDK12/Cyclin K molecular glue degraders, which were retrospectively found to stabilize protein-protein interactions through surficial ligand modifications not present in their non-glue analogs (*18-22, 54*). We reasoned that such modifications could be discovered prospectively by using parallelized chemical synthesis to resurface a protein-ligand complex at scale. Indeed, we and others have shown that the direct attachment of simple electrophilic handles can turn ligands into CIPs, further supporting this idea (*23, 24, 55*).

We used SuFEx transformations to establish an initial proof-of-concept, given (i) the wide commercial availability of SuFEx-compatible amine building blocks, (ii) the facile and scalable synthetic procedures used for large library builds, and (iii) the ability to perform an effector-agnostic screen by testing crude reaction products directly in native living systems. However, given our observation that the sulfamide of dHTC1 was essential for its activity, other chemistries will likely yield different hits, and it is therefore encouraging that additional high-throughput chemistries are available (*56-60*). Notably, DNA-encoded libraries have been used to identify bifunctional compounds with glue-like cooperativity, but these approaches demand that the target and effector both be pre-selected, as they are not compatible with cell-based screening techniques (*61, 62*).

At first, it seemed unlikely to have screened over 3,000 analogs for ENL only to discover a compound that operates through the known effector, CRBN, and even more improbable when considering that the compound possesses minimal independent affinity for the E3 ligase. However, this finding may bear on the question of whether there are intrinsic differences in the degree to which different ligases can be repurposed for targeted protein degradation. While genetic screens using fusion protein constructs have evaluated this *en masse* and found hundreds of proteins that can support targeted protein degradation (*63, 64*), recent discoveries of small-molecule degraders appear to repeatedly and independently converge on a common subset of effectors (*e.g.*, CRBN, DCAF11, DCAF16, and FBXO22) (*23, 28, 29, 55, 65-70*). It is intriguing to speculate whether this might reflect immutable characteristics of those proteins, such as their intrinsic ligandability or an evolved capacity to engage in protein-protein interactions with many diverse partners. It has been proposed that CRBN recognizes proteins with C-terminal cyclic imide modifications that are formed from the cyclization of asparagine and

glutamine on damaged proteins (*43*). This mechanism of degron recognition might suggest that CRBN is poised to bind a large fraction of the proteome, provided that it is presented with a cyclic imide modification for recognition (*43*). Our data might support this hypothesis, as ENL shows no binding to CRBN without dHTC1 but binds with high affinity through a distributed interface of protein-protein contacts when the spirosuccinimide of dHTC1 is presented on ENL.

Taken one step further, we might envision efforts to decorate ligands with cyclic imide moieties, regardless of their intrinsic affinity for CRBN, with the intent of discovering protein-ligand complexes that are biased for CRBN capture. For example, large collections of succinimide and glutarimide building blocks might be installed onto pre-existing ligands of interest to identify degraders that bind CRBN only in the presence of their target. These building blocks might even be incorporated into the design of large, diverse chemical screening libraries that would be biased for CRBN-capture without being biased for CRBN affinity. An extraordinary amount of effort has been dedicated toward assembling libraries of CRBN-biased ligands to discover new molecular glues (*13, 34, 71-78*), but these have relied on high-affinity CRBN ligands as starting points. (*S*)-dHTC1 suggests this is not necessary, as the pre-formed ENL-ligand complex can bind CRBN with high affinity. Conceptually, ENL can be considered an extension of the dHTC1 chemical scaffold, making its weak independent affinity for CRBN irrelevant. In fact, since the degradation of CRBN *neo*-substrates can be a major concern in the development of CRBN-based degraders (*16, 79-81*), a lack of independent CRBN affinity is likely a benefit that minimizes the chance of eliciting off-target *neo*-substrate degradation.

Incidentally, in addition to revealing a new mechanism to coopt CRBN for targeted protein degradation, dHTC1 also represents an exceptionally well-characterized chemical probe to study ENL biology that is differentiated from other ENL probes by its inactive enantiomeric control. Notably, such a stereoisomeric control is difficult to develop with thalidomide-based degraders, which are often prone to fast racemization *in situ* (*82*). The existence of an enantiomeric control, as well as the lack of off-target degradation events for this spirosuccinimide-based compound, positions (*S*)-dHTC1 favorably as a chemical probe for the study of ENL function in cellular and animal model systems.

Acknowledgements. This work was supported by the Ono Pharma Foundation Breakthrough Science Initiative Awards Program, the Baxter Foundation Young Investigator Award, the National Institutes of Health (NIH) Office of the Director (DP5-OD26380), and the National Cancer Institute (R01CA280720) (M.A.E.); a PhD Fellowship from the Boehringer Ingelheim Fonds (BIF) (M.M.O); the German Research Foundation (Deutsche Forschungsgemeinschaft, DFG) project number 511811315; United States National Science Foundation (CHE-2046286) (K.M.E.); and the National Institutes of Health K99GM138758 and R00GM138758 (S.K.). H.F. received funding from a Japan Society for the Promotion of Science (JSPS) Postdoctoral Fellowship, no. 23KJ1669. Funding is also gratefully acknowledged from the Innovative Medicines Initiative 2 (IMI2) Joint Undertaking under grant agreement no. 875510 (EUbOPEN project to A.C.). The IMI2 Joint Undertaking receives support from the European Union's Horizon 2020 research and innovation program, European Federation of Pharmaceutical Industries and Associations (EFPIA) companies, and associated partners KTH, OICR, Diamond, and McGill. We thank the Automated Synthesis Facility, the Nuclear Magnetic Resonance Core, and the Center for Metabolomics at The Scripps Research Institute. We thank Dr. George Tsaprailis at the Proteomics Core at The Herbert Wertheim UF Scripps Institute for aid in proteomics experiments. The authors thank the Core Facility Flow Cytometry of the Medical University of Vienna for access to flow cytometry instruments and assistance with cell sorting; the CeMM Biomedical Sequencing Facility for NGS sample processing, sequencing and data curation; J. Zuber and members of the Zuber laboratory for sharing KBM7 iCas9 cell lines and plasmids. We thank the staff of the Harvard Cryo-Electron Microscopy Center for Structural Biology for their technical expertise and support during grid screening and data collection. We acknowledge the SBGrid consortium for assistance with structural biology software packages and high-performance computing. X-Ray crystallography was supported by Proposal mx35324 at Diamond Light Source and beamline scientists at I24. Molecular graphics and analyses performed with UCSF ChimeraX, developed by the Resource for Biocomputing, Visualization, and Informatics at the University of California, San Francisco, with support from National Institutes of Health R01-GM129325 and the Office of Cyber Infrastructure and Computational Biology, National Institute of Allergy and Infectious Diseases.

Competing Interest Statement. M.A.E. and S.K. are inventors on a patent application related to SR-0813 and TM-7. M.A.E. and J.B.S. are inventors on a patent application related to dHTC1. M.A.E holds equity in Nexo Therapeutics and serves on their scientific advisory board. G.E.W. is a scientific founder and shareholder of Proxygen and Solgate and on the Scientific Advisory Board of Nexo Therapeutics. The Winter lab has received research funding from Pfizer. E.S.F. is a founder, scientific advisory board (SAB) member, and equity holder of Civetta Therapeutics, Proximity Therapeutics, Stelexis Biosciences, and Neomorph, Inc. (also board of directors). He is an equity holder and SAB member for Avilar Therapeutics, Photys Therapeutics, and Ajax Therapeutics and an equity holder in Lighthorse Therapeutics, CPD4, Inc and Anvia Therapeutics. E.S.F. is a consultant to Novartis, EcoR1 capital, Odyssey and Deerfield. The Fischer lab receives or has received research funding from Deerfield, Novartis, Ajax, Interline, Bayer and Astellas. A.C. is co-founder and shareholder of Amphista Therapeutics, a company that develops targeted protein degradation platforms. The Ciulli laboratory receives or has received sponsored research support from Almirall, Amgen, Amphista Therapeutics, Boehringer Ingelheim, Eisai, Merck KgaA, Nurix Therapeutics, Ono Pharmaceutical and Tocris-Biotechne. B.F.C. and B.M. are founders and/or scientific advisors to Magnet Biomedicine.

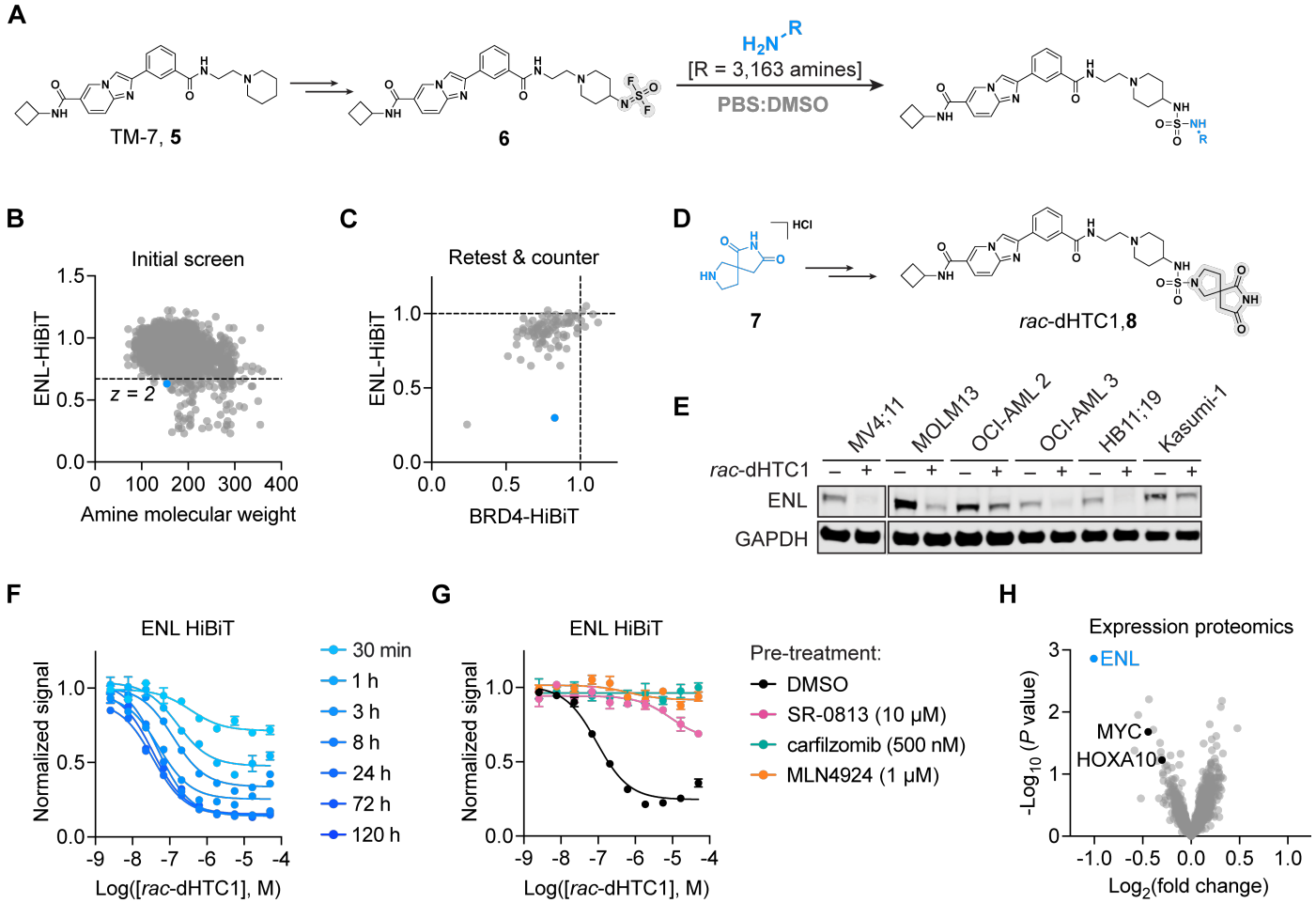

Figure 1. Prospective discovery of *rac*-dHTC1 by high-throughput chemical diversification. (**A**) TM-7 (**5**) with an iminosulfur oxydifluoride SuFEx handle (**6**) was used for the parallel synthesis of 3,163 analogs. (**B**) Crude reaction products were screened for ENL degradation (5 μM, 24 h) in MV4;11 cells expressing HiBiT-ENL. HiBiT luminescence normalized to DMSO:PBS vehicle control (n = 1). Molecular weight shown for the free amine coupling partner. (**C**) Resynthesized hits were rescreened by HiBiT-ENL (n = 3) and counter screened against BRD4-HiBiT (n = 3). HiBiT luminescence normalized to DMSO:PBS vehicle control. (**D**) Chemical structure of building block **7** and *rac*-dHTC1 (**8**). (**E**) Immunoblot of ENL in AML cell lines treated with purified *rac*-dHTC1 (10 μM, 24 h) or DMSO vehicle control. (**F**) Time-dependent and dose-responsive loss of HiBiT-ENL signal in MV4;11 cells treated with *rac*-dHTC1. Luminescence normalized to DMSO vehicle control (n = 4). (**G**) Dose-responsive effects of *rac*-dHTC1 in MV4;11 cells following indicated pretreatments (1 h). HiBiT-ENL luminescence normalized to DMSO vehicle control (n = 4). Data in **Fig. S4B** are taken from the same experiment (DMSO pre-treatment is repeated in both panels) (**H**) Quantitative TMT-based expression proteomics analysis of MV4;11 cells treated with *rac*-dHTC1 (1μM, 16 h) or DMSO vehicle control (5,512 proteins with >2 peptides, data was filtered using DTAselect 2.0 within IP2). P values were calculated with a two-tailed Student's t-test, (n = 3).

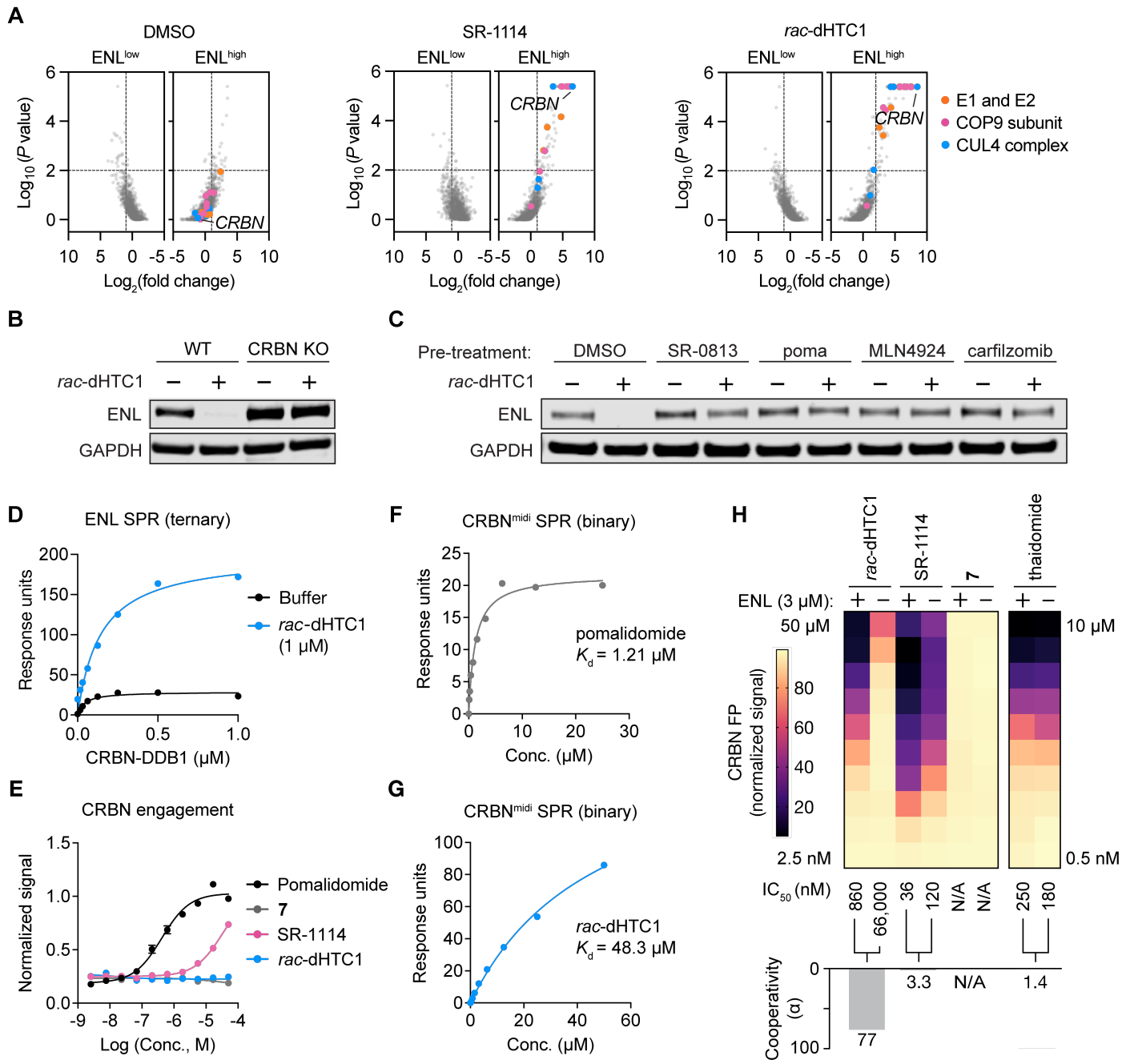

Figure 2. ENL degradation by *rac*-dHTC1 proceeds through CRL4^{CRBN} despite minimal CRBN affinity. (**A**) FACS-based CRISPR screens for UPS components affecting ENL stability in KBM7 reporter cells (ENL-BFP-P2A-mCherry) treated with DMSO, SR-1114 (10 μM) or *rac*-dHTC1 (10 μM) for 8 h (6 sgRNAs targeting 1301 UPS-associated genes). Gene-level fold change and *P* values were determined by one-sided MAGeCK analysis. (**B**) Immunoblot analysis of wild-type and CRBN-deficient MV4;11 cells treated with *rac*-dHTC1 (10 μM, 6 h) or DMSO vehicle control. (**C**) Immunoblot analysis of MV4;11 cells pretreated with DMSO vehicle control, SR-0813 (10 μM), pomalidomide (poma, 25 μM), MLN4924 (1 μM) or carfilzomib (500 nM) for 1 h prior to *rac*-dHTC1 treatment (10 μM, 6 h) or DMSO vehicle control. (**D**) SPR analysis of CRBN-DDB1 binding to immobilized ENL-YEATS in the presence of *rac*-dHTC1 or buffer control. (**E**) Rescue of dBET6-mediated BRD4 degradation to assess CRBN target engagement. MV4;11 cells expressing BRD4-HiBiT were pretreated with compounds in dose response for 2 h prior to a 1 h treatment with dBET6 (500 nM, n = 3). Data for pomalidomide is repeated below in **Fig. S6E**, which originated from a single experiment. (**F**) SPR analysis of pomalidomide binding to immobilized CRBN^{midi}. (n = 1). (**G**) *rac*-dHTC1 (same as **F**). (**H**) Heatmap depicting normalized CRBN FP signal following treatment with the indicated compounds, In the presence of ENL (3 μM) or buffer control (n = 1). Cooperativity values are calculated from the ratio of IC_{50} values with and without ENL.

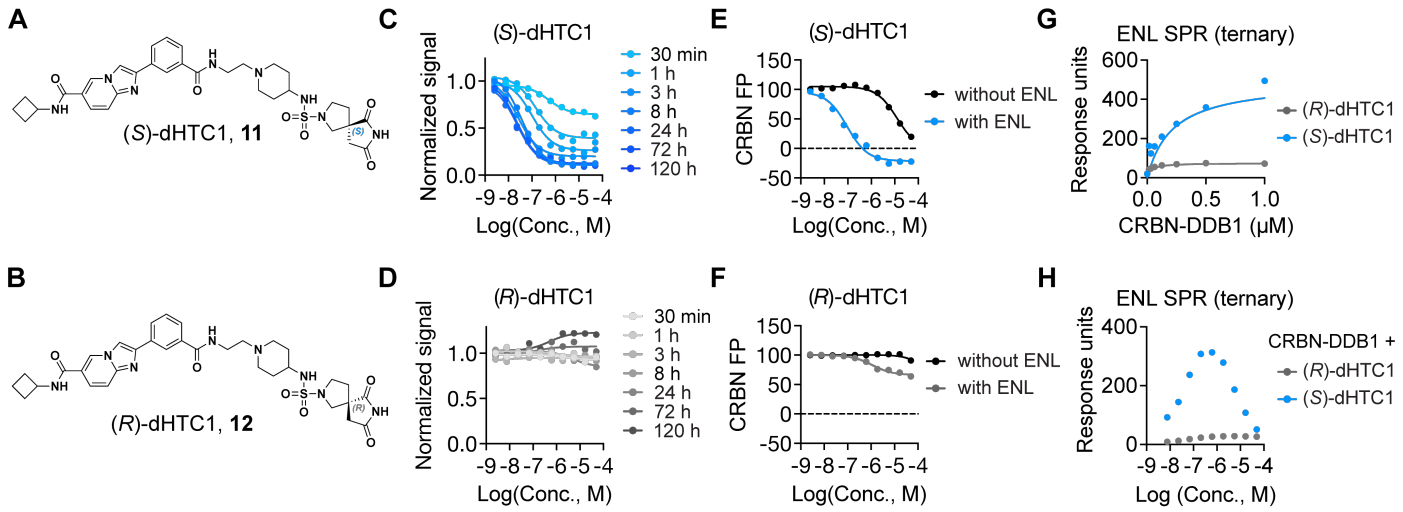

Figure 3. The pre-formed ENL:(*S*)-dHTC1 complex binds cooperatively and stereoselectively to CRBN. (**A**), (**B**) Structures of dHTC1 enantiomers. (**C**) Luminescence-based measurement of HiBiT-ENL abundance in MV4;11 cells treated with (*S*)-dHTC1 (normalized to DMSO control, n = 4) (**D**) (*R*)-dHTC1 (same as **C**). (**E**) CRBN-DDB1 FP assay measuring (*S*)-dHTC1 displacement of BODIPY-thalidomide (10 nM) from CRBN-DDB1 (50 nM) in the presence of recombinant ENL YEATS protein (3 μM) or buffer control. (**F**) (*R*)-dHTC1 (same as **E**). (**G**) SPR analysis of immobilized ENL YEATS binding to CRBN-DDB1 (dose response) combined with (*S*)- or (*R*)-dHTC1 (1 μM). (**H**) SPR analysis of immobilized ENL YEATS binding to (*S*)- or (*R*)-dHTC1 (dose response) combined with CRBN-DDB1 (500 nM). (*S*)-dHTC1 with CRBN-DDB1 is partially repeated in **Fig. S6F** (data are taken from the same experiment).

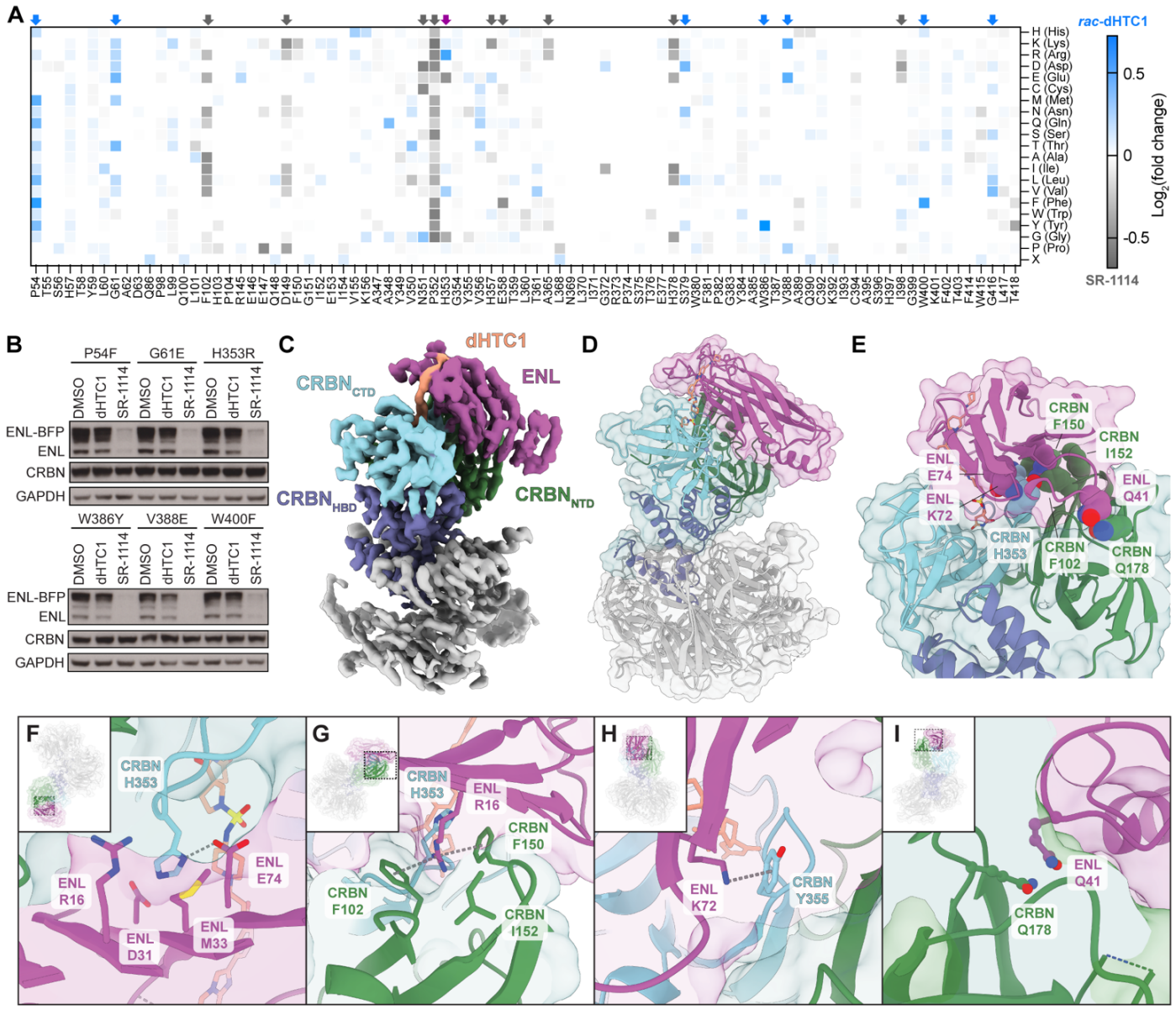

Figure 4. (*S*)-dHTC1 mediates extensive protein-protein contacts between ENL and CRBN. (**A**) Heat map comparing CRBN DMS results for *rac*-dHTC1 and SR-1114. C-terminal ENL-BFP levels in MV4;11 CRBN$^{-/-}$ ENL-TagBFP-P2A-mCherry cells were measured by flow cytometry following transduction with a CRBN DMS library and drug treatment (dHTC1 or SR-1114, 1 μM for 8h, n = 3). Arrows above indicate residues showing selectivity for dHTC1 (blue), SR-1114 (gray), or mixed (purple) that were selected for follow-up assays. (**B**) Immunoblot analysis of MV4;11 CRBN$^{-/-}$ ENL-TagBFP-P2A-mCherry cells expressing the indicated CRBN mutation treated with dHTC1 or SR-1114 (1 μM for 6h). Images are re-used in **Fig. S8D**. (**C**) EM map of DDB1:CRBN bound to (*S*)-dHTC1 and ENL colored by protein. (**D**) Model of DDB1:CRBN bound to (*S*)-dHTC1 and ENL complex. (**E**) View of CRBN-ENL interface with select contacting residues shown with space-filling representations. (**F-I)** Views of select CRBN and ENL residues making intermolecular protein-protein contacts.

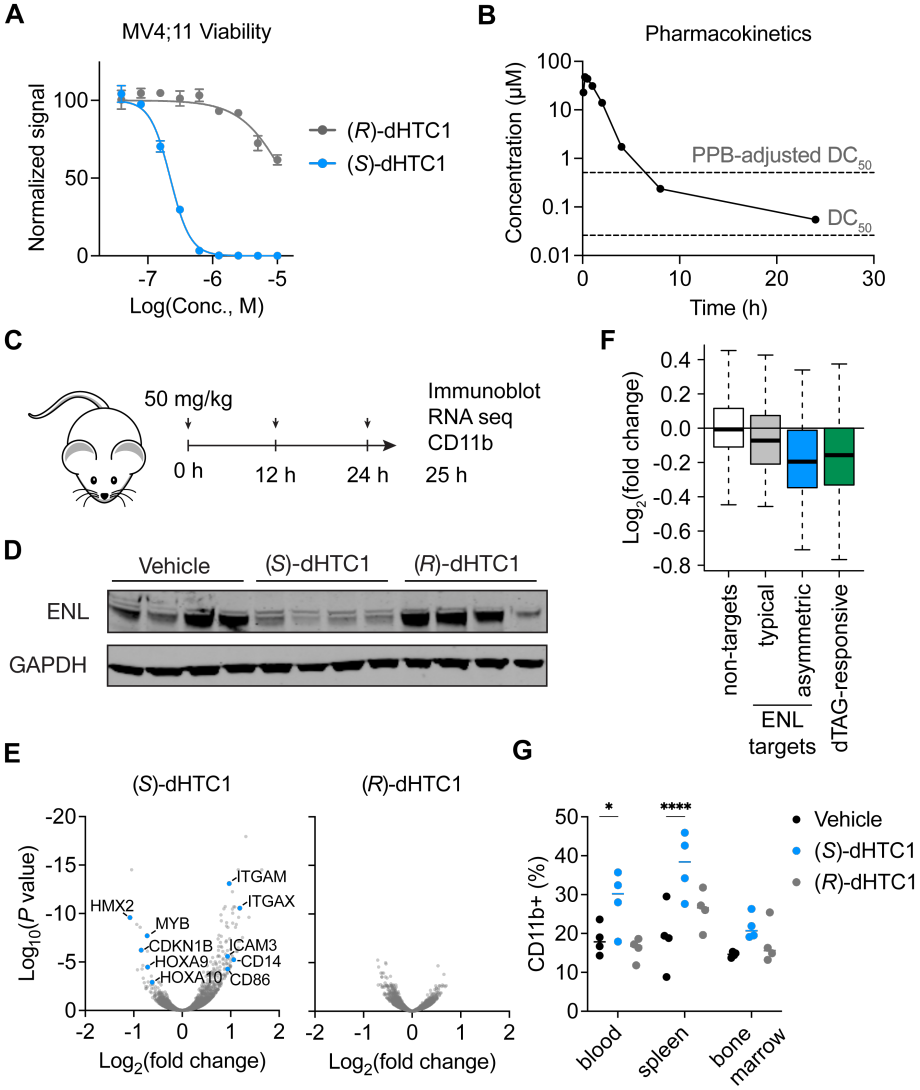

Figure 5. Stereoselective degradation of ENL *in vivo*. (**A**) Viability of MV4;11 cells after 12-d treatment with (*S*)-dHTC1 or (*R*)-dHTC1 measured by ATP-dependent luminescence (normalized to DMSO, *n* = 3). (**B**), Mean plasma concentration of (*S*)-dHTC1 in male C57BL/6 mice dosed with 50 mg/kg via intraperitoneal injection (*n* = 3). Cellular DC_{50} (MV4;11 at 8 h) is depicted with and without adjustment for percent protein binding (PPB). (**C**) Diagram representing the timeline of dosing and data collection for *in vivo* studies. (**D**) Immunoblot analysis of mouse-cell-depleted bone marrow from MV4;11 xenotransplantations following treatment with vehicle, (*S*)-dHTC1 (50 mg/kg), or (*R*)-dHTC1 (50 mg/kg) via intraperitoneal injection (*n* = 4 mice per group). (**E**) RNA-seq analysis of mouse-cell-depleted bone marrow lysates from MV4;11 xenograft (3 individual mice per treatment condition from xenograft experiment shown in figure **5D**). (**F**) Box and whisker plot depicting the effect of (*S*)-dHTC1 on the mRNA expression of ENL target genes compared to vehicle control. ENL target genes defined by typical (grey, *n* = 176) and asymmetric (blue, *n* = 56) ENL ChIP-seq signal strength within the gene promoter region or by responsiveness to ENL degradation via dTAG-enabled chemically induced degradation (green, *n* = 150). Non-targets include all other expressed transcripts (*n* = 14,854). Boxes indicate first to third quartiles and whiskers represent 1.5X the interquartile range. (**G**) Flow cytometry-based quantification of CD11b expression in indicated tissues (same mice as in **Fig. 5D**).

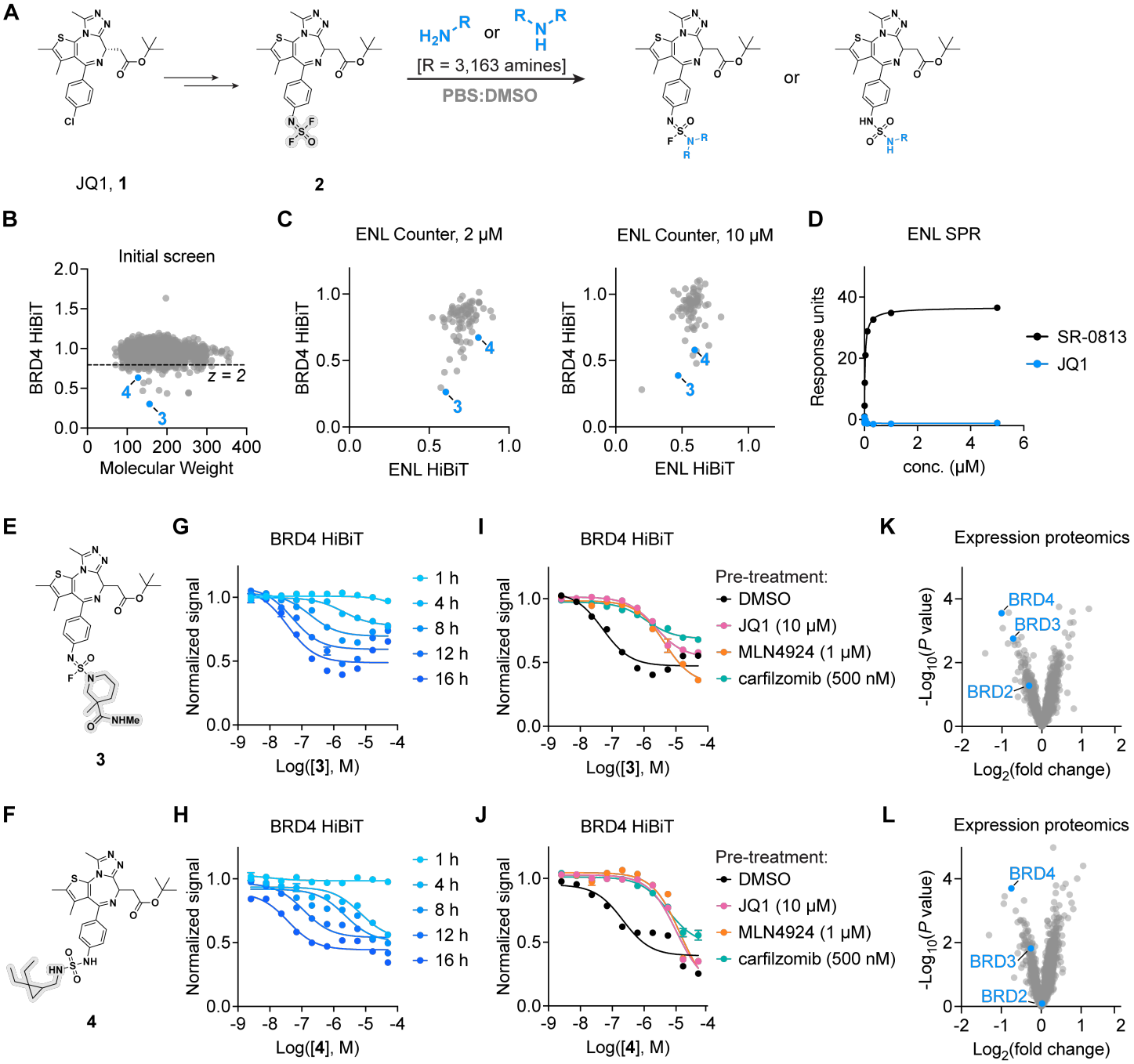

Figure S1. Prospective discovery of BRD4 degraders by high-throughput chemical diversification. (**A**) JQ1 (**1**) with an iminosulfur oxydifluoride SuFEx handle (**2**) used for parallel synthesis of 3,163 analogs. (**B**) Crude reaction products were screened for BRD4 degradation (2 μM, 16 h) in MV4;11 cells expressing BRD4-HiBiT. HiBiT luminescence normalized to DMSO:PBS vehicle control (n = 1). Molecular weight shown for the free amine building block. (**C**) Hits were rescreened at 2 or 10 μM (16 h) in MV4;11 BRD4-HiBiT (n = 3) and counter screened against MV4;11 ENL-HiBiT (n = 3). HiBiT luminescence normalized to DMSO:PBS vehicle control. (**D**) ENL-YEATS affinity determination using SPR (n = 1). Data from **Fig. S2C** are taken from the same experiment (SR-0813 data is repeated in both panels). (**E**) Structure of **3**. (**F**) Structure of **4**. (**G**) Time-dependent and dose-responsive loss of BRD4-HiBiT signal in MV4;11 cells treated with **3**. Luminescence normalized to DMSO vehicle control (n = 4). (**H**) Same as **G**, treatment with **4**. (**I**) Dose-responsive effects of **3** in MV4;11 cells (12 h) following the indicated pretreatment for 1 h. HiBiT-ENL luminescence normalized to DMSO vehicle control (n = 4). (**J**) Same as **I**, treatment with **4**. (**K**) Quantitative TMT-based expression proteomics analysis of MV4;11 cells treated with **3** (1μM, 16 h) or DMSO vehicle control (5,400 proteins with >2 peptides depicted, data was filtered using DTAselect 2.0 within IP2). P values were calculated with a two-tailed Student's t-test, n = 3. (**L**) Same as **K**, treatment with **4**.

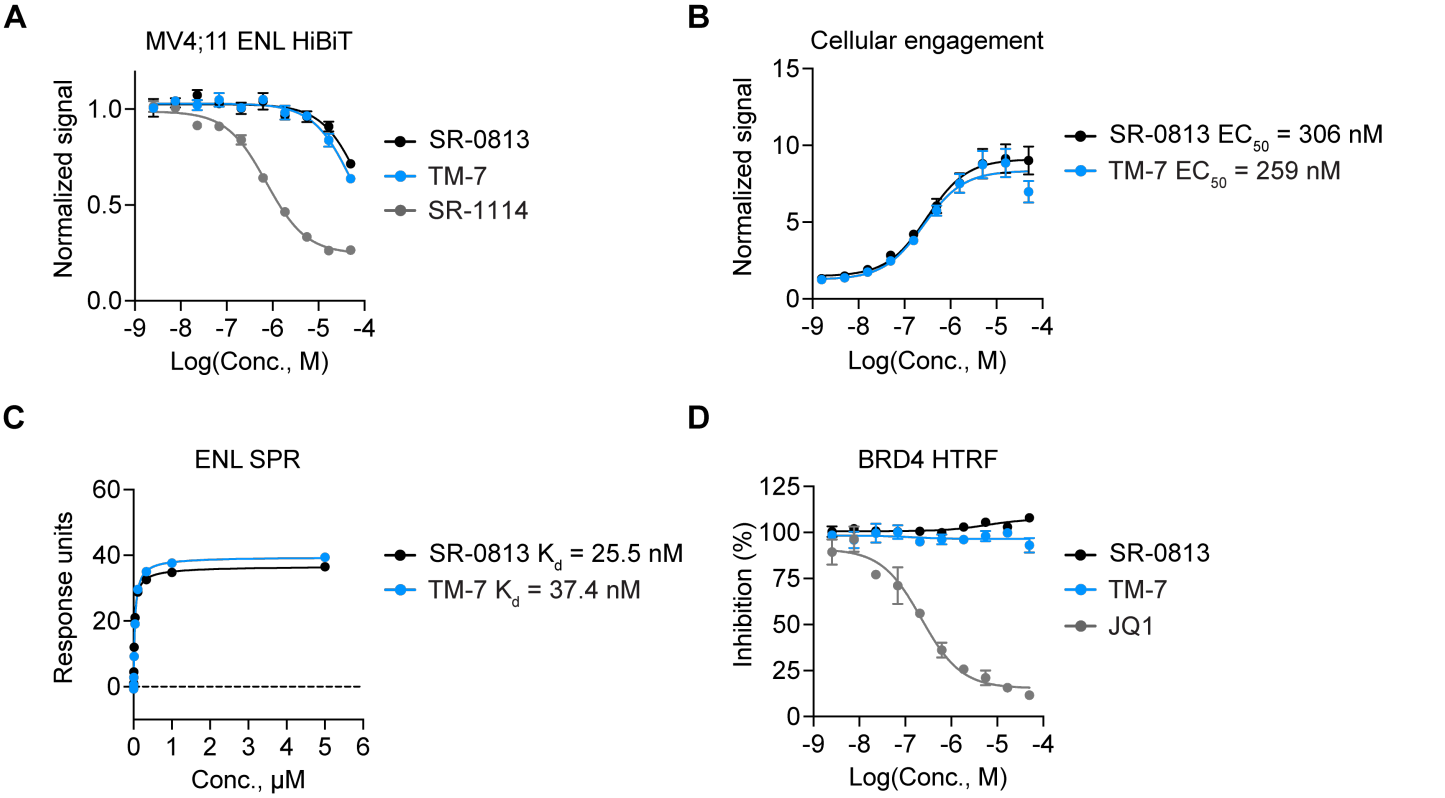

Figure S2. TM-7 is a high affinity ligand for the ENL YEATS domain. (**A**) DMSO-normalized HiBiT signal in ENL-HiBiT expressing MV4;11 cells following 24 h treatments (*n* = 4). (**B**) Intracellular engagement of ENL-YEAT by TM-7 and SR-0813 (*n* = 4). (**C**) ENL-YEATS affinity determination using SPR (*n* = 1). Data from **Fig. S1D** are taken from the same experiment (SR-0813 data is repeated in both panels). (**D**) Activity of ENL inhibitors against BRD4, as measured by homogenous time resolved fluorescence (HTRF) (*n* = 3).

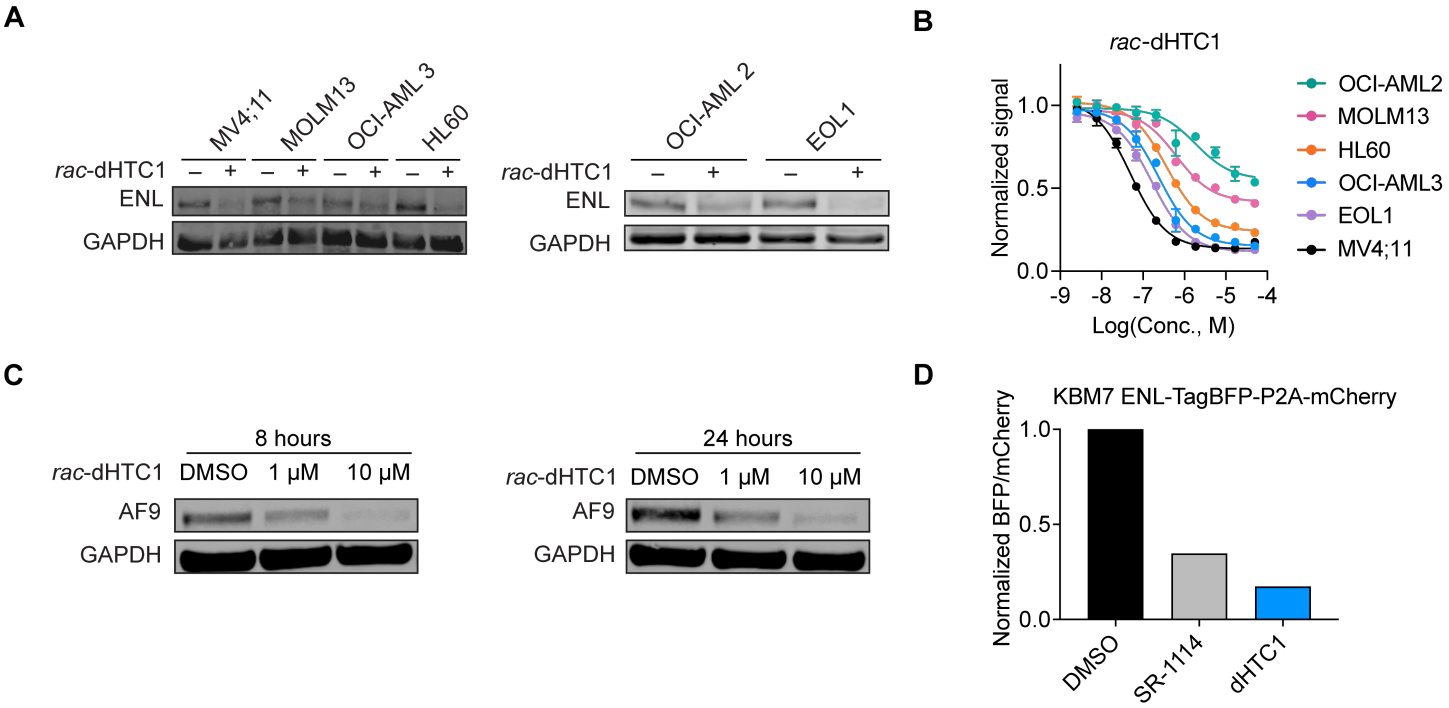

Figure S3. *rac*-dHTC1 degrades ENL and AF9 in leukemia cell lines. (**A**) Immunoblot analysis of ENL in a panel of AML cell lines treated with 10 μM *rac*-dHTC1 or DMSO control for 24 hours. (**B**) ENL-HiBiT expressing AML cell lines treated with *rac*-dHTC1 for 24 hours. Signal is normalized to DMSO treated cells (n = 4). (**C**) Immunoblot analysis of AF9 levels in Jurkat cells treated with *rac*-dHTC1 or DMSO control. (**D**) Validation of an ENL reporter construct. KBM7 cells expressing an ENL-TagBFP-P2A-mCherry dual fluorescence stability reporter were treated with 10 μM compound or DMSO control for 8 h (n = 1).

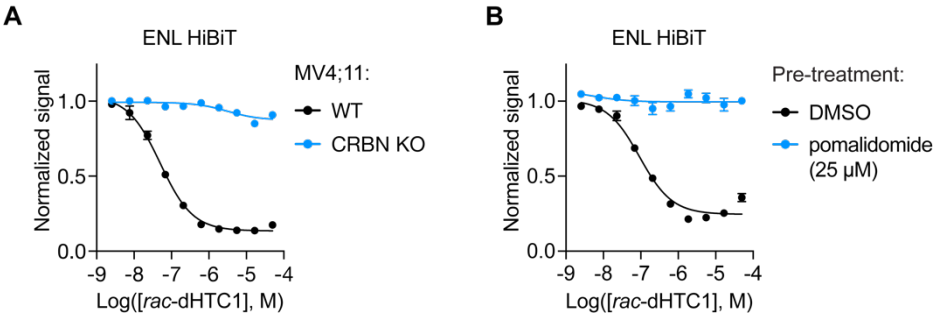

Figure S4. CRBN-dependent degradation of ENL by dHTC1. (**A**) HiBiT-ENL response to *rac*-dHTC1 treatment (24 h) in wild-type and CRBN-deficient MV4;11 cells. Luminescence normalized to DMSO vehicle control (n = 4). (**B**) MV4;11 HiBiT-ENL cells pretreated with pomalidomide (25 μM, 1 h) or DMSO control prior to *rac*-dHTC1 treatment (24 h). Luminescence normalized to DMSO vehicle control (n = 4). Data in **Fig. 1G** are taken from the same experiment (DMSO pre-treatment is repeated in both panels).

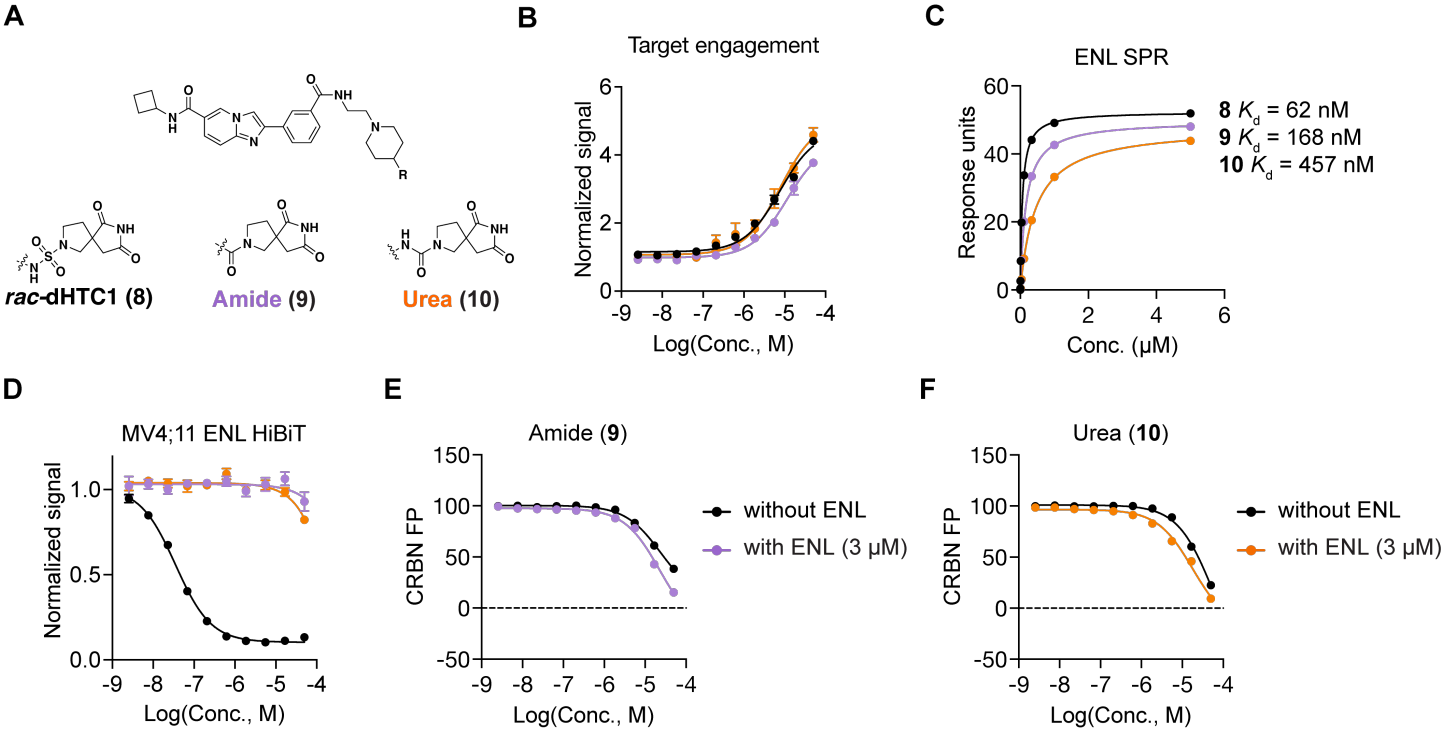

Figure S5. Close structural analogs of dHTC1 do not induce ENL degradation. (**A**) Structure of dHTC1 analogs. (**B**) HiBiT-based intracellular ENL-YEATS target engagement assay (3 h). MLN4924 pre-treatment (1 μM, 1 h) was used to prevent the potential for compound-induced degradation. Signal is normalized to DMSO-treated cells (n = 4). Data in **Fig. S6D** is taken from the same experiment (*rac*-dHTC1 data is repeated in both panels). (**C**) Binding to immobilized ENL-YEATS as measured by SPR (n = 1). Data in **Fig. S6C** is taken from the same experiment (*rac*-dHTC1 data is repeated in both panels). (**D**) HiBiT-based ENL degradation assay (24 h). Signal is normalized to DMSO treated cells (n = 4). (**E**) CRBN FP assay for **9** in the presence of recombinant ENL YEATS domain (3 μM) or buffer. (**F**) Urea analog **10** (same as **E**) (n = 1).

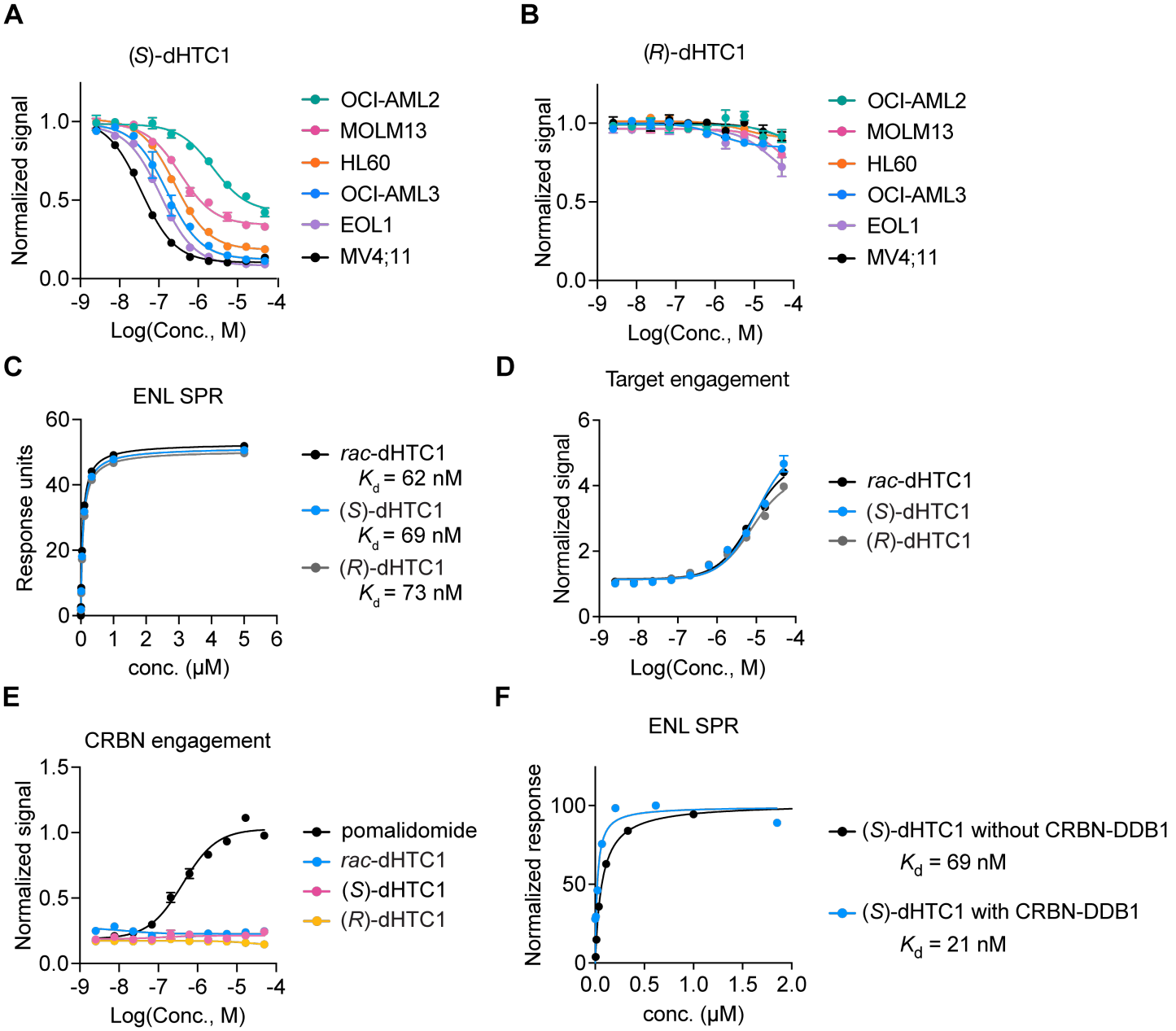

Figure S6. Stereoselective effects of dHTC1 enantiomers. (**A**) HiBiT-based ENL degradation assay in cells expressing HiBiT-ENL and treated with (*S*)-dHTC1 (24 h). Signal is normalized to DMSO treated cells (n = 4). (**B**) The same as (**A**) but for (*R*)-dHTC1. (**C**) Binding to ENL as measured by SPR (n = 1). Data in **Fig. S5C** is taken from the same experiment (*rac*-dHTC1 data is repeated in both panels). (*S*)-dHTC1 binding curve is repeated in **Fig. S6F**. (**D**) HiBiT-based intracellular ENL-YEATS target engagement assay (3 h). Cells were pretreated with MLN4924 (1 μM, 1 h) to prevent the potential for compound-induced degradation. Signal is normalized to DMSO-treated cells (n = 4). Data in **Fig. S5B** is taken from the same experiment (*rac*-dHTC1 data is repeated in both panels). (**E**) Intracellular CRBN target engagement assessed in MV4;11 cells expressing BRD4-HiBiT via rescue of dBET6-induced BRD4 degradation. Cells are pretreated with compounds in dose response for 2 h prior to a 1-h treatment with dBET6 (500 nM, n = 3). Data for pomalidomide is repeated above in **Fig. 2E**, which originated from a single experiment. (**F**) (*S*)-dHTC1 binding to ENL measured by SPR, with or without CRBN-DDB1 (500 nM) present (n = 1). Each trace is normalized to its response at saturation. (*S*)-dHTC1 without CRBN-DDB1 data is repeated from **Fig. 3H**.

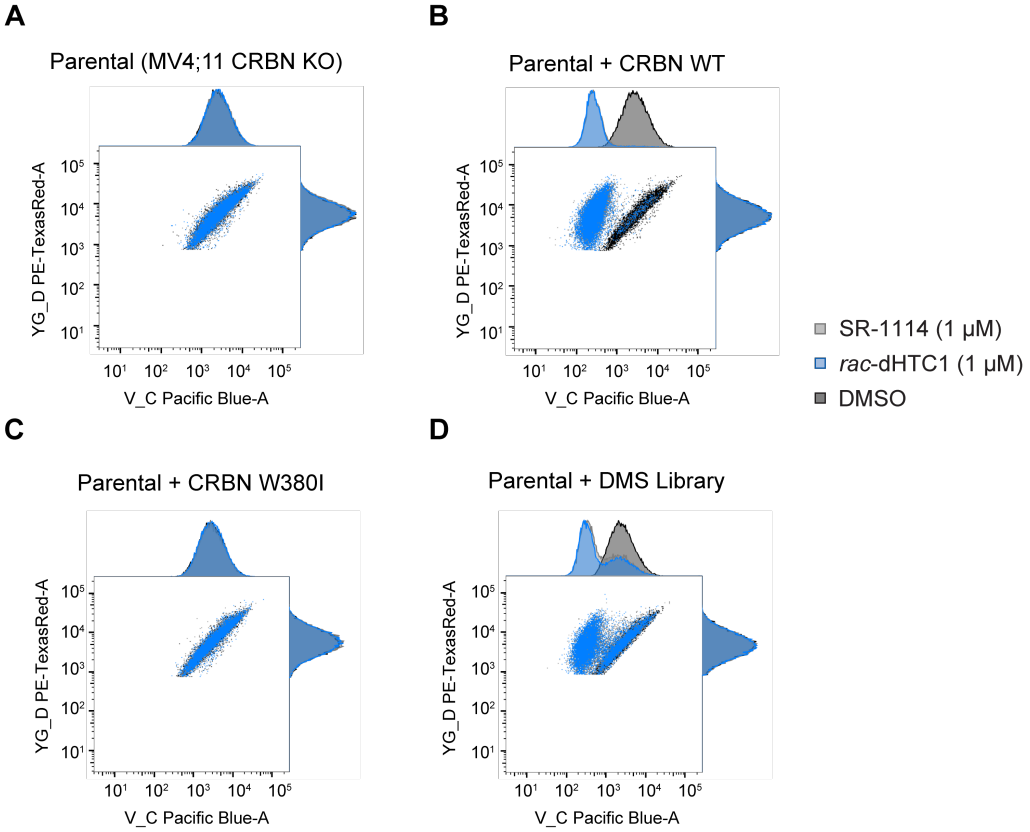

Figure S7. Validation of MV4;11 cell line for CRBN DMS screen. (**A**) Flow cytometry following drug treatment in MV4;11 CRBN knockout cells expressing a BFP-tagged ENL and P2A-separated mCherry internal control. This cell line is defined as the "parental." The histograms for SR-1114, *rac*-dHTC1 and DMSO treated cells overlap because ENL degradation is CRBN-dependent. (**B**) Control demonstrating that the reintroduction of wild-type CRBN restores ENL degradation to drug-treated cells. (**C**) Control demonstrating that the reintroduction of CRBN with an inactivating mutation (W380I) fails to mediate ENL degradation. (**D**) Cells that were transduced with the CRBN DMS library regained activity, with roughly 70% of the cells showing ENL degradation.

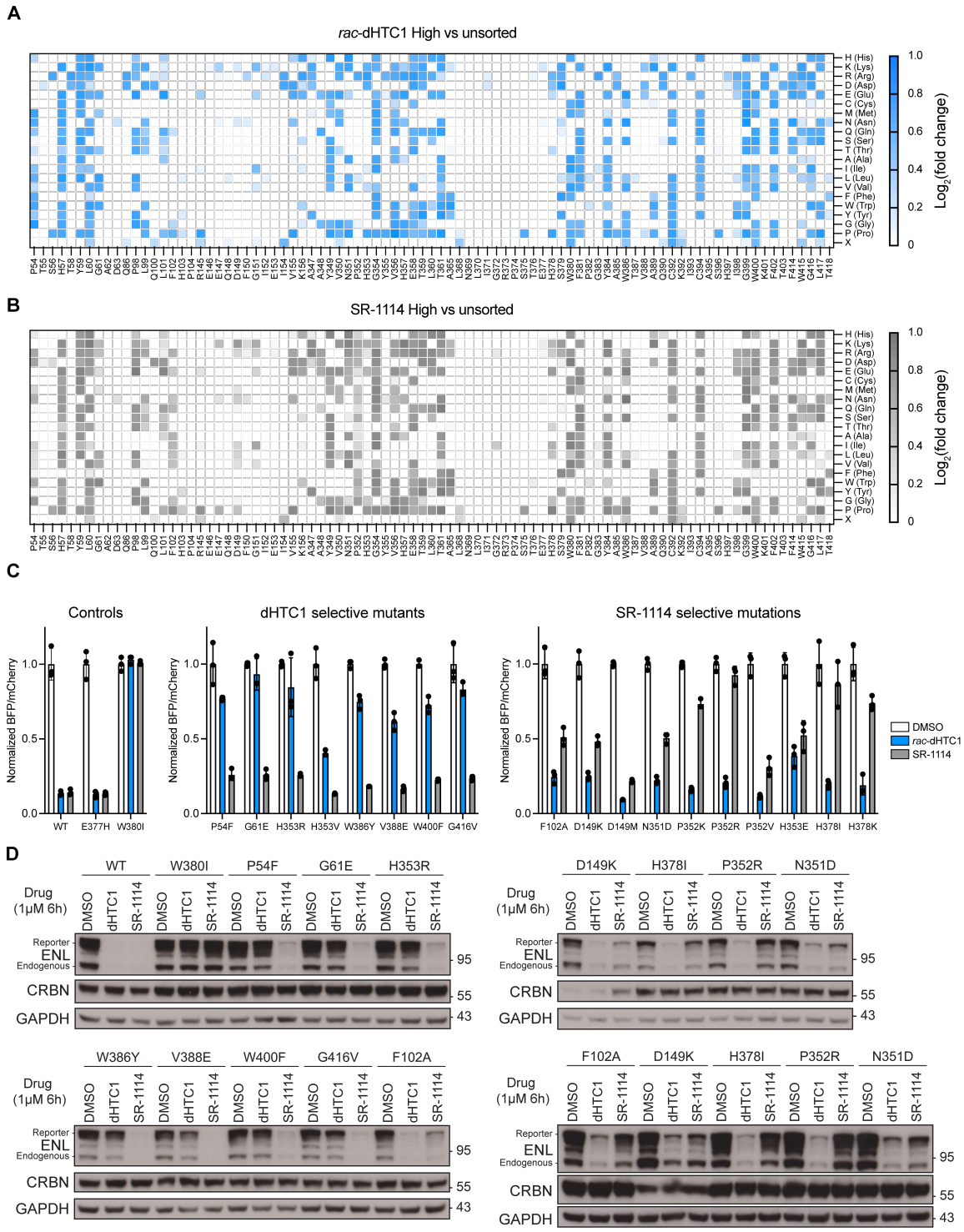

Figure S8. Validation of CRBN DMS results. (**A**) MV4;11 CRBN knockout cells expressing ENL-TagBFP-P2A-mCherry were transduced with a DMS library, which reintroduced CRBN with single amino acid mutations within a 10 Å radius of the thalidomide binding site. After these cells were treated with *rac*-dHTC1 (1 μM, 8 h, n = 3), endpoint ENL levels were quantified by flow cytometry. Results are depicted in a heatmap indicating $\log_2$ fold change of ENL^{high} over the unsorted pools. (**B**) SR-1114 (same as **A**). (**C**) Validation results of individually expressed CRBN mutants assessed by flow cytometry (n = 3). (**D**) Immunoblot analyses of ENL levels in MV4;11 CRBN knockout cells expressing ENL-TagBFP-P2A-mCherry. Wild-type or mutant CRBN was re-introduced by lentiviral expression to evaluate mutations that selectively impact the ability of dHTC1 or SR-1114 to degrade ENL (1 μM, 6 h). For ENL, the lower molecular weight band is the endogenous protein and the higher molecular weight band is the reporter construct. Sections of this figure are also shown in **Fig. 4B**.

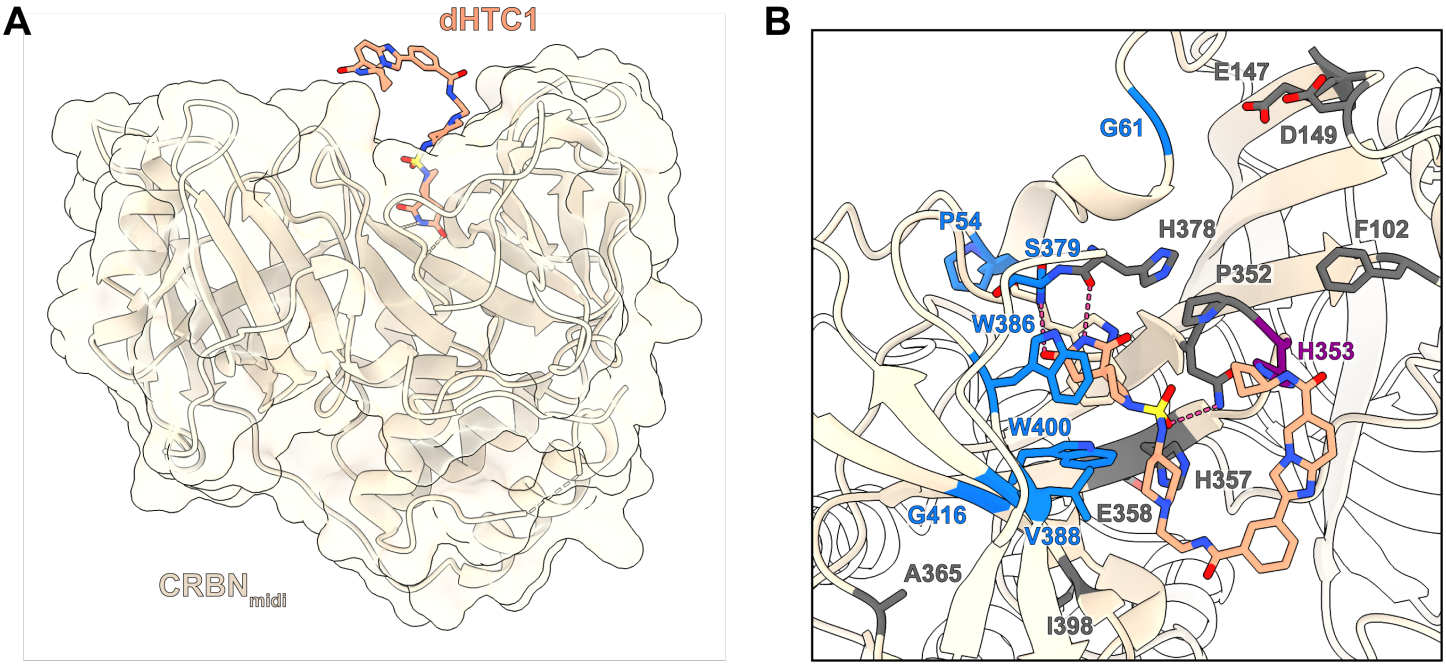

Figure S9. Structural features of dHTC1 bound to CRBN. (**A**) Co-crystal structure of (*S*)-dHTC1 bound to CRBN^{midi}. (**B**) View of the IMiD-binding site bound by (*S*)-dHTC1. Residues indicated with an arrow in **Figure 4A** are colored accordingly.

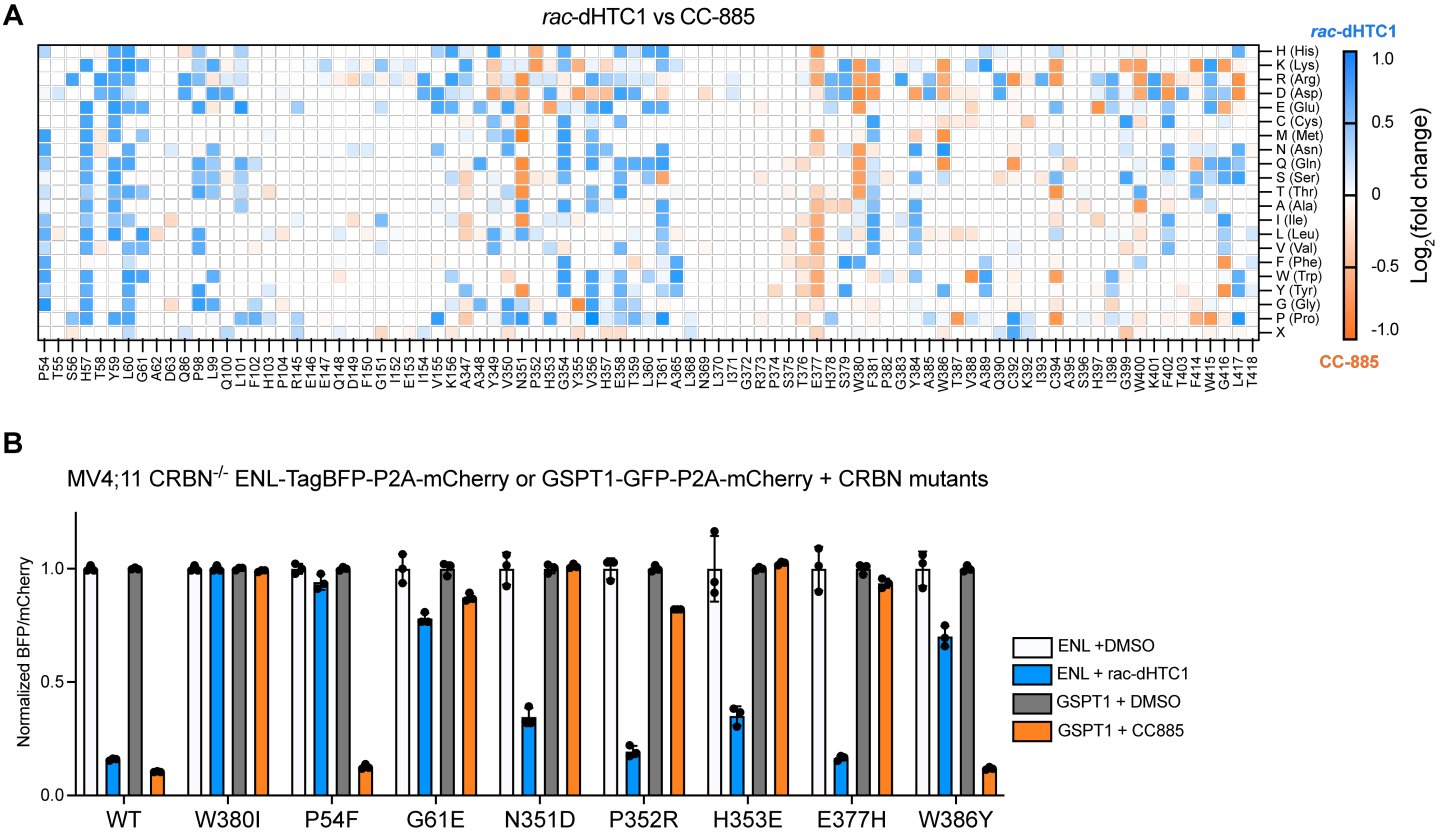

Figure S10. Comparison of CRBN DMS results for dHTC1 and CC-885. (**A**) Differential activity between CC-885 (500 nM, 7 d) treated RKO cells (*49*) and dHTC1 (1 μM, 8 h) treated MV4;11 ENL-TagBFP-P2A-mCherry cells. (**B**) Validation of selected CRBN mutations in MV4;11 CRBN$^{-/-}$ GSPT1-GFP-P2A-mCherry treated with CC-885 versus ENL-TagBFP-P2A-mCherry treated with (n = 3).

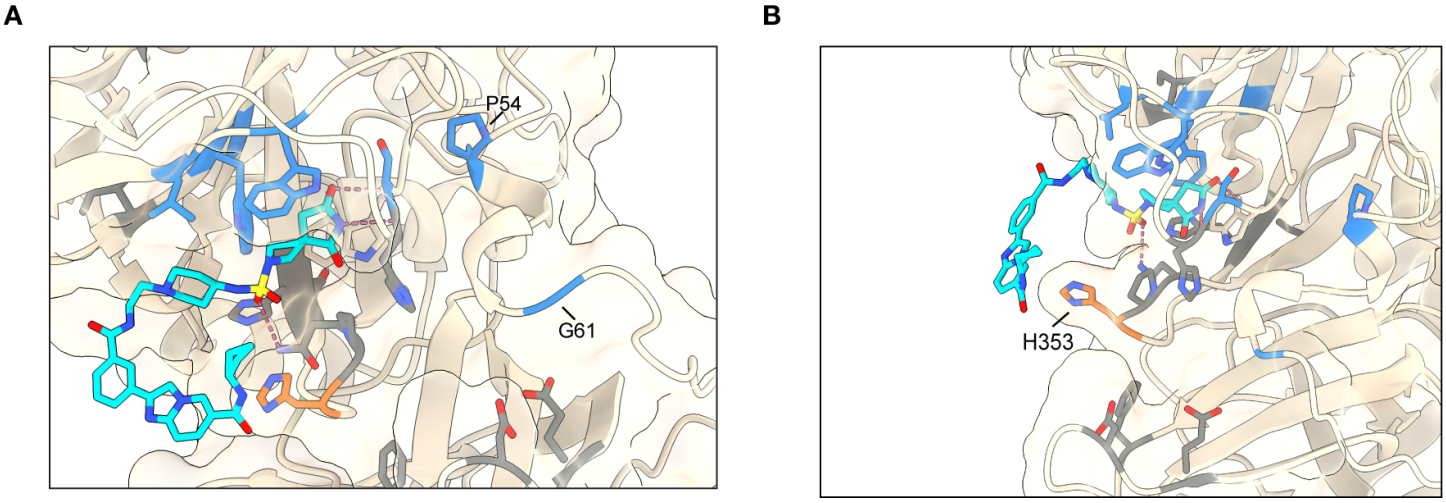

Figure S11. Distal CRBN amino acid residues that impact dHTC1 activity. (**A**) View of P54 and G61, distal (> 10 Å) to the dHTC1 binding pocket. (**B**) View of H353.

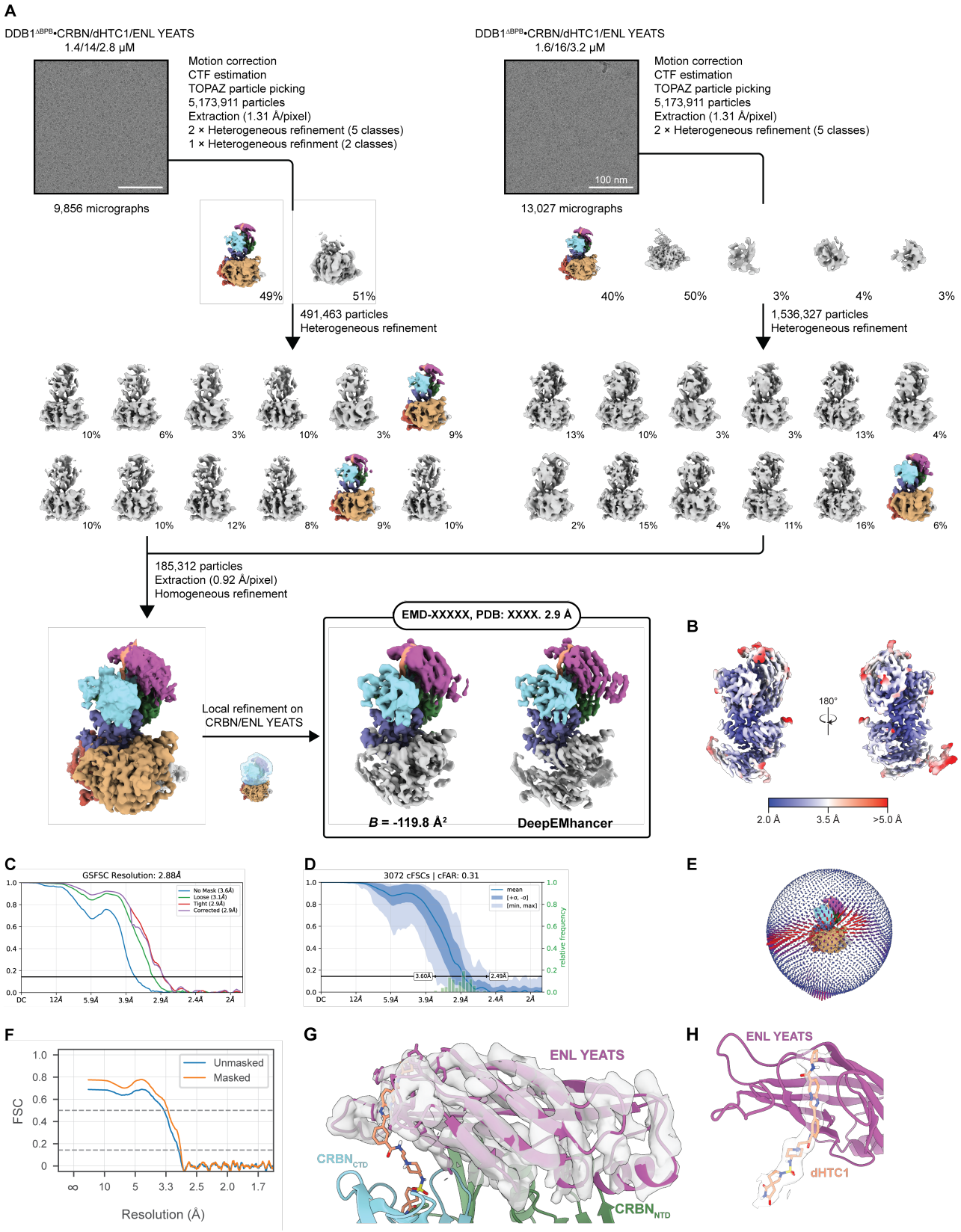

Fig. S12. Cryo-EM processing workflow for the CRBN•ENL YEATS structure. (**A**) Overview of processing workflow from raw micrograph (scale bar indicated) to final maps. Particles belonging to colored volumes were taken into subsequent steps. Contour levels of maps after homogeneous refinement, local refinement, and postprocessing with DeepEMhancer are 0.025, 0.03, and 0.10 respectively. (**B**) Local resolution mapped onto final map postprocessed by DeepEMhancer (**C**) FSC plot, (**D**) Directional FSC plot. (**E**) Viewing distribution. (**F**) Model-to-map FSC for XXXX in EMD-XXXXX. (**G, H**) Cryo-EM density examples (threshold 0.10) for ENL YEATS and dHTC1 (map postprocessed by DeepEMhancer).

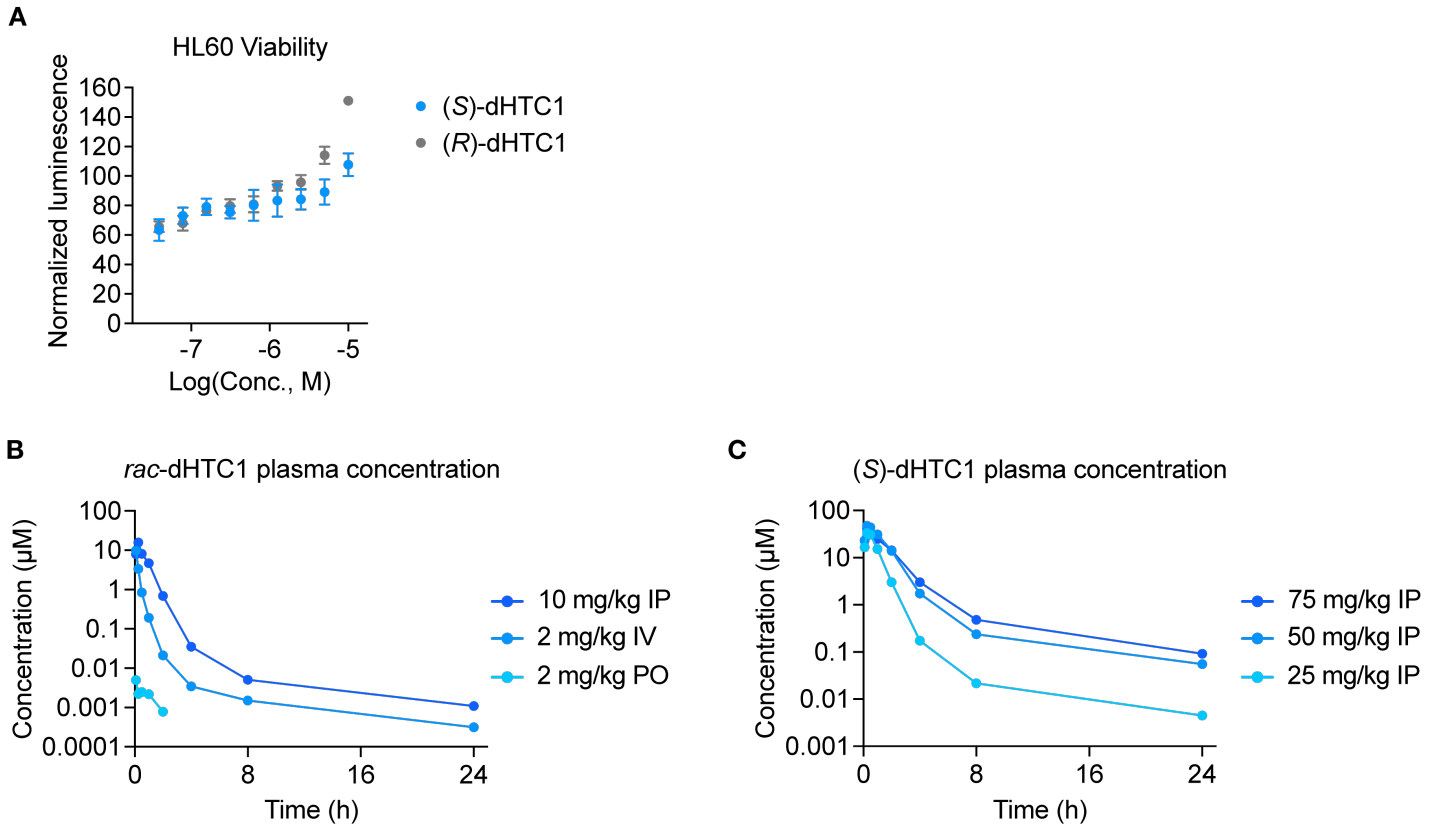

	2 mg/kg IV	2 mg/kg PO	10 mg/kg IP
T_{max} (h)	0.083	0.083	0.250
C_{max} (ng/mL)	6703	3.37	10673
$T_{1/2}$ (h)	6.13	0.858	4.57

	25 mg/kg	50 mg/kg	75 mg/kg
T_{max} (h)	0.333	0.333	0.250
C_{max} (ng/mL)	23466	32667	27400
$T_{1/2}$ (h)	3.70	2.64	3.57

Figure S13: Assessment of dHTC1 *in vitro* and *in vivo*. (**A**) Viability of HL60 cells after 12 d treatment with (*S*)-dHTC1 or (*R*)-dHTC1 measured by CellTiterGlo (normalized to DMSO treated cells, $n = 3$). (**B**) Mean plasma concentration of male C57BL/6 mice dosed with *rac*-dHTC1 at 10 mg/kg via intraperitoneal (IP) injection, 2 mg/kg via intravenous (IV) injection or 2 mg/kg *per os* (PO) ($n = 3$). (**C**) Mean plasma concentration of male C57BL/6 mice dosed with 25, 50 or 75 mg/mg via intraperitoneal injection ($n = 3$). 50 mg/kg data is repeated from **Fig. 5B** (all data taken from the same experiment).

MATERIALS AND METHODS

Cell Lines and Culture

The following cell lines were used in this work: HL-60, OCI-AML-2, OCI-AML-3, HB11;19, MV4-11, MOLM-13, Kasumi-1, EOL1, KBM7 iCas9, K562, KBM7, Lenti-X 293 T and HEK293T. All cell lines were cultured in RPMI-1640, IMDM or DMEM media containing 10% or 20% heat-inactivated fetal bovine serum (FBS) and were supplemented with streptomycin and penicillin and stored at 37°C at 5% CO_2. HB11;19, MV4;11, MOLM13 and EOL1 cell lines were cultured in 10% FBS in RPMI-1640. OCI-AML-2, OCI-AML-3, Kasumi-1, and CMK cell lines were cultured in 20% FBS in RPMI-1640. HEK293T and Lenti-X 293 T cell lines were cultured in 10% FBS in DMEM. HL-60 and KBM7 cells were cultured in IMDM supplemented with 10% FBS. Commercial cell lines were obtained from ATCC or DSMZ and underwent authentication using short tandem repeat (STR) DNA profiling to confirm their identity prior to use. HB11;19 cell lines were generously provided by Akihiko Yokoyama. KBM7 iCas9 cells were a gift from J. Zuber. All cell lines were confirmed mycoplasma negative at 1-month intervals.

For lentiviral production, Lenti-X 293 T cells were seeded in 6-well plates or 10cm dishes and transfected at approximately 80% confluency with 0.6/3.4ug target plasmid, 1.7/0.3ug psPAX2 (Addgene 12260) and 0.85/0.15ug pMD2.G (Addgene 12259) using PEI (PolySciences). Virus supernatant was collected after 60h, filtrated using 0.45µm filter and stored in aliquots for transduction.

Viability Studies

To assess drug response, 20 x 10^4 MV4;11 or HL-60 cells were seeded per well in a non-tissue culture treated 96-well plate (VWR) and treated with 0.1% DMSO or increasing concentrations of (*R*)- or (*S*)-dHTC1 (39.07nM, 78.13nM, 156nM, 312nM, 625nM, 1.25µM, 2.5µM, 5µM and 10µM). Cells were split 1:10 and fresh drug was added every 3 days. Cell proliferation was measured on day 12 using the CellTiterGlo® Luminescent Cell Viability Assay (Promega). Drug response was calculated based on luminescence relative to the DMSO treated samples. The experiment was independently repeated 3 times in technical replicates and for each, the average luminescence was calculated. Diagrams show the mean of the 3 experiments and error bars represent the standard error of means (SEM).

ENL-HiBiT cell lines

The following cell lines were generated bearing an endogenously tagged N-terminal ENL HiBiT via homology directed repair: OCI-AML2, OCI-AML3, MV4;11 (WT and CRBN KO (*34*)), MOLM-13, EOL1, and HL60 . All components necessary were ordered from Integrated DNA Technologies. A Neon Transfection System (ThermoFisher) was used to electroporate cells. Briefly, sgRNA complexes are synthesized by mixing equal volumes of crRNA (2 µL, 160 µM in nuclease free water, ggcgccagccatggacaatc) and tracrRNA (2 µL, 160 µM) and are incubated at 37 °C for 30 min before Cas9 (2.7 µL, 10 µg/µL, Alt-R™ S.p. Cas9 Nuclease V3, catalog number 1081058) and duplex buffer (1.3 µL, 30 mM HEPES, pH 7.5; 100 mM potassium acetate in nuclease free water) are added. This suspension is incubated at 37 °C for an additional 15 min to form the active RNP complex. The RNP solution (1 µL) is added to ssODN (2 µM in nuclease free water, gcggcggcggcgagcgacgcggggcccgggggcggggcggggcgccagccatggtgagcggctggcggctgttcaagaagattagcggaagcgg agacaatcaagtgaggagcggccgcgccgcccctgcgcagcccgcccggcccccct). The resulting mixture is electroporated with 200,000 cells in electroporation buffer and the cells are deposited into antibiotic free media (see *Cell Lines and Culture* for conditions) and allowed to rest in a 37 °C incubator for 24 h before additional antibiotic containing media is added. Replicates with the highest overall signal are selected and expanded.

The electroporation conditions for each cell lines were as follows: MV4;11, OCI-AML2, OCI-AML3, MV4;11, MOLM-13, EOL1: 1600 pulse voltage, 10 millisecond pulse width, 3 pulses. HL-60: 1350 pulse voltage, 35 millisecond pulse width, 1 pulse.

MV4;11 BRD4-HiBiT cell lines

All components necessary were ordered from Integrated DNA Technologies. A Neon Transfection System (ThermoFisher) was used to electroporate cells. Briefly, sgRNA complexes are synthesized by mixing equal volumes of crRNA (2 µL, 160 µM in nuclease free water, aatcttttctgagcgcacct) and tracrRNA (2 µL, 160 µM) and are incubated at 37 °C for 30 min before Cas9 (2.7 µL, 10 µg/µL, Alt-R™ S.p. Cas9 Nuclease V3, catalog number 1081058) and duplex buffer (1.3 µL, 30 mM HEPES, pH 7.5; 100 mM potassium acetate in nuclease free water) are added. This suspension is incubated at 37 °C for an additional 15 min to form the active RNP complex. The RNP solution (1 µL) is added to ssODN (2 µM in nuclease free water, catgaatttccagagtgatctattgtcaatatttgaagaaaatcttttcggtggcggtggctcgggcggtggtgggtcgggtggcggcggatctgtgagcggct ggcggctgttcaagaagattagctgacctaggtggcttctgactttgattttctggcaaaacattgactttccata). The resulting mixture is electroporated (1600 pulse voltage, 10 millisecond pulse width, 3 pulses) with 200,000 cells in electroporation buffer and the cells are deposited into antibiotic free media (see *Cell Lines and Culture* for conditions) and allowed to rest in a 37 °C incubator for 24 h before additional antibiotic containing media is added. Replicates with the highest overall signal are selected and expanded.

Endpoint HiBiT protein degradation

MV4;11 cells were engineered using CRISPR knock-in of the HiBiT tag at the n-terminus of ENL and the c-terminus of BRD4 with a protocol adapted from the Neon™ Transfection System Quick Reference. Cells were seeded into 384-well plates at 20,000 cells/well and treated with the indicated compounds and equivalent concentrations of DMSO for the time indicated in the experiment, usually 3, 24 or 72 hours. Levels of HiBiT-tagged proteins were detected via luminescence using the Nano-Glo® HiBiT Lytic Detection System (Promega, catalog number N3050). Dose response curves were fitted using non-linear regression and the data shown are from n = 3 or n = 4 independent repeats, mean plus or minus standard error of the mean.

ENL Intracellular engagement assay

Intracellular ENL engagement assays were carried out as described previously (*83*). Briefly, an Echo acoustic liquid handler (Labcyte) was used to transfer drug in 10-point dose response (100 nL transfers) to empty wells on a white, tissue culture treated 384 well plate. To these wells were added OCI/AML-2 cells stably expressing ENL(YEATS)-HiBiT at concentrations of 20,000 cells in 20 µL of media. The plate was placed on an orbital shaker for 15 seconds and was then placed in a 37 °C incubator for 3 h, or a time otherwise indicated, after which each well was treated with 20 µL of Nano-Glo® HiBiT Lytic Detection (Promega, N3050). After this treatment, the plate is mixed with an orbital shaker for 15 seconds and allowed to rest in the dark for 20 min before luminescence is measured with a Clariostar microplate reader (BMG Labtech). Luminescence values are normalized to DMSO treated wells and dose response curves were fitted using non-linear regression.

CRBN Intracellular engagement assay

An Echo acoustic liquid handler (Labcyte) was used to transfer drug in 10-point dose response (100 nL transfers) to empty wells on a white, tissue culture treated 384 well plate. MV4;11 cells stably expressing an endogenous BRD4 with a C-terminal HiBiT (*34*) were added at concentrations of 20,000 cells in 18 µL of media, and the plate was mixed on an orbital shaker for 15 seconds. The plate was placed into a 37 °C incubator for 2 hours before 2 µL of a 5 µM dBET6 solution in RPMI with 10% FBS was added to each well, and the plate was again placed on an orbital shaker for 15 seconds (final concentration of dBET6 is 500 nM, control wells are treated with an equal volume of DMSO in RPMI with 10% FBS). After 1 h incubation at 37 °C, each well was treated with 20 µL of Nano-Glo® HiBiT Lytic Detection (Promega, N3050). After this treatment, the plate is mixed with an orbital shaker for 15 seconds and allowed to rest in the dark for 20 min before luminescence is measured with a Clariostar microplate reader (BMG Labtech). Luminescence values are normalized to DMSO treated wells and dose response curves were fitted using non-linear regression.

Western blotting

For adherent cell lines, cells were plated in 6 or 12-well plates at approximately $1x10^6$ cells per well and allowed to adhere overnight. For suspension lines, cells were plated at $1x10^6$ cells per well and used shortly thereafter. Wells were treated with the indicated compounds for the times indicated in each experiment. Cells were then

washed with ice cold PBS and lysed with 1X RIPA buffer supplemented with protease inhibitor and phosphatase inhibitor (Life Technologies). Lysates were sonicated and centrifuged, and the supernatants were collected. Protein concentration in cell lysates was measured using BCA assay. 25 µg of denatured total protein from each sample was separated by sodium dodecyl sulfate-polyacrylamide gel electrophoresis (SDS-PAGE) using 4-12% Bis-Tris gels and transferred to nitrocellulose membranes. Membranes were blocked with 5% milk in TBST and then incubated with primary antibodies overnight at 4 °C (all antibodies were 1:1000 in 5% milk in TBST, while GAPDH primary antibody is diluted 1:5000 in 5% milk in TBST). Bound primary antibodies were incubated in the appropriate secondary antibody (IRDye680 goat-anti-mouse: 925-68070, IRDye800 goat-anti-rabbit: 926-32211, diluted 1:5000 in 5% milk in TBST). Secondary antibodies are incubated at room temperature for 90 minutes before being washed with additional TBST and are visualized on an Odyssey CLx (LI-COR Biosciences).

Alternatively, MV4;11 CRBN$^{-/-}$ ENL-TagBFP-P2A-mCherry cells rescued with CRBN wild-type or mutant were seeded in 12-well plates at 1x10^{6} cells per mL and treated with DMSO, 1µM dHTC1 or 1µM SR-1114 for 6h. Cells were washed twice in ice-cold PBS and lysed for 15min on ice with RIPA buffer (50mM Tris-HCl pH 8.0, 150mM NaCl, 1% Triton X-100, 0.5% sodium deoxycholate, 0.1% SDS) supplemented with benzonase protease (25U/mL) and 1x Halt protease inhibitor cocktail. Following clearance via centrifugation, protein concentration of lysates was determined using Pierce BCA Protein Assay (23225, Fisher Scientific) and 30µg of lysate was prepared using 4x LDS sample buffer (Thermo Fisher) and 10% 2-mercaptoethanol and run on NuPAGE 4-15% bis-tris gels (Thermo Fisher). Proteins were transferred to nitrocellulose membranes, blocked for 30min in 5% milk TBS-T at room temperature before incubating with primary antibodies for 1h at room temperature. The following primary antibodies were used: ENL (1:1,000, D9M4B, Cell Signaling Technology) CRBN (1:2,000, gift of R. Eichner and F. Bassermann) and GAPDH (1:2,000, FL-335, Santa Cruz Biotechnology). Membranes were then washed in TBS-T and incubated with horseradish peroxidase (HRP)-conjugated secondary antibodies for 45 min at room temperature before further washes and developing with chemiluminescence films. Secondary antibodies used: peroxidase-conjugated AffiniPure Goat Anti-Rabbit IgG (1:10,000, Jackson ImmunoResearch, 111-035-003) and peroxidase-conjugated AffiniPure Goat Anti-Mouse IgG (1:10,000, Jackson ImmunoResearch, 115-035-003).

For western blots of xenografted MV4;11 cells, mouse cell depletion was performed on whole bone marrow cells using the Mouse Cell Depletion Kit and LS columns (Miltenyi Biotec). RIPA lysis was performed with purified human cells and 25µg of protein were loaded on 10% Bis-Tris-Gel NuPAGE gels with MOPS SDS running buffer (Life Technologies). Samples were transferred on nitrocellulose iBlot 3 transfer stacks (Life Technologies) using the iBlot 3 Gel Transfer Device (Thermo Fisher). Membranes were blocked in 5% milk in TBS-Tween buffer (TBST) for one hour at room temperature and incubated overnight at 4°C with antibodies directed against ENL (Millipore, 1:1000 in 5% milk in TBST) or GAPDH (Cell Signaling Technologies, 1:1000 in 5% milk in TBST). Membranes were washed followed by incubation with the secondary IRDye 800CW donkey anti-rabbit antibody (Thermo Fisher Scientific, 1:7000 in 5% milk in TBST) for one hour at room temperature and subsequent washes were performed. Membranes were imaged on a LI-COR imager.

Primary Antibodies Used:
ENL: D9M4B (Cell Signaling Technologies) or ABE2596-100UG (Millipore)
AF9: E5Z7U (Cell Signaling Technologies)
GAPDH: sc-32233 (Santa Cruz Biotechnology)
Secondary Antibodies Used:
Goat anti-Mouse IgG with IRDye 680RD: 925-68070 (LI-COR)
Goat anti-Rabbit IgG with IRDye 800CW: 926-32211 (LI-COR)
Goat anti-Rabbit IgG with HRP: 111-035-003 (Jackson ImmunoResearch)
Goat anti-Mouse IgG with HRP: 115-035-003 (Jackson ImmunoResearch)
Donkey anti-Rabbit with IRDye800CW: 926-32213 (LI-COR)

Expression Proteomics
The mass spectrometry proteomics data have been deposited to the ProteomeXchange Consortium via the PRIDE (*84*) partner repository with the dataset identifier PXD055068.

Sample Preparation

Treated cells were resuspended in 200 µL of cold DPBS containing protease inhibitor (cOmplete ULTRA tablets mini EDTA-free, Roche, Cat # 05892791001, 1 tablet was dissolved in 10 mL DPBS before use). Cells were lysed by probe sonication using a Branson Sonifer 250 ultrasonic cell disruptor (2 x 12 pulses, 10% power output). Protein content of whole cell lysates was determined using the DC protein Assay (Bio-Rad, Cat # 5000113 and 5000114) with absorbance at 750 nm measured on a CLARIOstar plate reader. A volume corresponding to 200 µg of protein was transferred to a new low-bind Eppendorf tube containing 48 mg of urea and brought to a total volume of 100 µL. Samples were reduced with DTT by the addition of 5 µL of a 200 mM solution (10 mM final concentration) and were incubated at 65 °C for 15 minutes. Samples were next alkylated with iodoacetamide by the addition of 5 µL of a 400 mM solution (20 mM final concentration) and incubated at 37 °C for 30 minutes in the dark. Proteins in each sample were precipitated by the addition of cold MeOH (500 µL), $CHCl_3$ (100 µL) and H_2O (400 µL). Samples were vortexed and centrifuged (16000 g, 10 minutes, 4 °C). The supernatant was aspirated leaving behind the protein disc and an additional 1 mL of cold MeOH was added. The samples were vortexed again and centrifuged (16000 g, 10 minutes, 4 °C). The supernatant was aspirated and the protein pellet was briefly allowed to air dry. The protein pellet was then resuspended in 160 µL of EPPS buffer (200 mM, pH 8.0) by probe sonication (10 pulses, 10% power output). Proteomes were digested with Lys-C by the addition of 4 µL of a 0.5 µg/µL Lys-C solution in HPLC-grade water and the samples were incubated for 2 hours at 37 °C. Proteomes were then digested with trypsin by the addition of 8 µL of a 0.5 µg/µL trypsin solution in trypsin resuspension buffer with 20 mM $CaCl_2$ and the samples were incubated at 37 °C overnight. Peptide concentrations were determined using a Micro BCA™ assay (Thermo Scientific, Cat # 23235) and a volume that corresponded to 25 µg was transferred to a new low-bind Eppendorf tube and brought to a total volume of 25 µL with EPPS buffer. To each sample, 9 µL of HPLC-grade acetonitrile was added followed by 3 µL (20 µg/µL in dry acetonitrile) of the respective TMT^{6plex} tag and the reaction was vortexed and incubated at room temperature for 1 hour with additional vortexing every 20 minutes. The reaction was quenched by the addition of 6 µL of 5% hydroxylamine in H_2O, vortexed, and incubated at room temperature for 15 minutes. Each sample was acidified by the addition of 2.5 µL of LCMS-grade formic acid. Samples were combined by taking 25 µL of each sample (~12.5 µg of labeled peptide per channel) and vacuum-centrifuged. The combined samples were desalted with a Sep-Pak C18 cartridge and offline-fractionated by HPLC.

Sample de-salting and offline fractionation

Samples were resuspended in 500 µL of buffer A (95% H_2O, 5% acetonitrile, 0.1% formic acid), vortexed and water bath sonicated for 5 minutes at room temperature. Before loading the sample onto a Sep-Pak C18 cartridge (Waters, Cat # WAT054955), the column was conditioned with acetonitrile (3 x 1 mL) and equilibrated with buffer A (3 x 1 mL). The sample was then loaded onto the column and the flow through of the sample was added onto the column again. The sample was de-salted by adding buffer A (3 x 1 mL) and passing it through and the sample was then eluted by the addition of 1 mL of buffer B (80% acetonitrile, 20% H_2O, 0.1% formic acid). The eluted sample was collected into a new low-bind Eppendorf tube and was evaporated to dryness using a SpeedVac vacuum concentrator.

The sample was then resuspended in 500 µL of buffer A and fractionated using an Agilent HPLC (Agilent Infinity 1260 II system) into a 96 deep-well plate containing 20 µL of 20% formic acid as previously reported (*85, 86*). The peptides were eluted onto a capillary column (ZORBAX Extend-C18, 80 Å, 4.6 x 250 mm, 5 µM) and separated at a flow rate of 0.5 mL/min using the following gradient with buffer A (10 mM aqueous NH_4HCO_3) and buffer B (100% Acetonitrile): 100% buffer A from 0–2 min, 0–13% buffer B from 2–3 min, 13–42% buffer B from 3–60 min, 42–100% buffer B from 60–61 min, 100% buffer B from 61–65 min, 100–0% buffer b from 65–66 min, 100% buffer A from 66–75 min, 0–13% buffer B from 75–78 min, 13–80% buffer B from 78–80 min, 80% buffer B from 80–85 min, 100% buffer A from 86–91 min, 0–13% buffer B from 91–94 min, 13–80% buffer B from 94–96 min, 80% buffer B from 96–101 min, and 80–0% buffer B from 101–102 min. The eluent collected in the 96 deep-well plate was evaporated to dryness using a SpeedVac vacuum concentrator. The peptides were resuspended in 80% acetonitrile with 0.1% formic acid buffer and combined into 12 fractions (fractions were combined down a column of the plate) by addition 200 µL of buffer, resuspending by pipetting, and combining into the next row. This process was repeated with another 200 µL. Each of the fractions had a final volume of 400 µL and were evaporated to dryness using a SpeedVac vacuum concentrator.

TMT liquid chromatography-mass-spectrometry (LC-MS) analysis

Dried fractions were solubilized in 50mL of 0.1% trifluoroacetic acid and desalted using 2µg capacity ZipTips (Millipore, Billerica, MA) according to manufacturer instructions. Peptides were then on-line eluted into a Fusion Tribrid mass spectrometer (Thermo Scientific, San Jose, CA) from an EASY PepMap^{TM} RSLC C18 column (2µm, 100Å, 75µm x 50cm, Thermo Scientific, San Jose, CA), using a hold of 6% solvent B (80/20 acetonitrile/water, 0.1% formic acid) for 15 minutes, followed by a gradient of 6-28% solvent B in 105 minutes, then 28-49% solvent B in 15 minutes, 40-100% solvent B in 10 minutes, a 10 minute hold of 100% solvent B, a return to 5% solvent B in 3 minutes, and finally a 3 minute hold of 5% solvent B. The gradient was then extended for the purpose of cleaning the column by increasing solvent B to 100% in 3 min, a 100% solvent B hold for 10 min, a return to 5% solvent B in 3 min, a 5% solvent B hold for 3 min, an increase of solvent B again to 100% in 3 min, then a 100% solvent B hold for 10min, a return to 5% solvent B in 3 minutes, a 5% solvent B hold for 3 min and finally one last increase to 100% solvent B in 3 minutes and a hold of 100% solvent B for 10min. All flow rates were 250 nL/minute delivered using an nEasy-LC1000 nano liquid chromatography system (Thermo Scientific, San Jose, CA). Solvent A consisted of water and 0.1% formic acid. Ions were created at 2.0 or 1.9kV using an EASY Spray source (Thermo Scientific, San Jose, CA) held at 50 °C. A synchronous precursor selection (SPS)-MS3 mass spectrometry method was selected based on the work of Ting et al (*87*). Scans were conducted between 380-2000 m/z at a resolution of 120,000 for MS1 in the Orbitrap mass analyzer at a standard AGC target (as defined in Thermo Scientific Xcalibur v 4.6.67.17) and a maximum injection of 50 msec. Collision induced dissociation (CID) was then performed in the linear ion trap of peptide monoisotopic ions with charge 2-8 above an intensity threshold of 5E3, using a quadrupole isolation of 0.7 m/z and a CID energy of 35%. The ion trap AGC target was also set to standard with a maximum injection time of 50 msec. Dynamic exclusion duration was set at 60 seconds and ions were excluded after one time within the +/- 10ppm mass tolerance window. The top 10 MS2 ions in the ion trap between 400-1200 m/z were then chosen for Higher-energy C-trap dissociation (HCD) at 65% energy. Detection occurred in the Orbitrap at a resolution of 50,000 and an AGC target of 1E5 (or 200% custom setting as defined in Thermo Scientific Xcalibur v 4.6.67.17), and an injection time of 120msec (MS3). All scan events occurred within a 3-second specified cycle time. The analysis was performed at The Herbert Wertheim UF Scripps Institute for Biomedical Innovation & Technology, Mass Spectrometry and Proteomics Core Facility (RRID:SCR_023576).

Peptide and protein identification and quantification

The raw spectra files were uploaded to the Integrated Proteomics Pipeline (IP2) (http://ip2.scripps.edu/ip2/mainMenu.html) and MS2 and MS3 files were extracted from the raw files using RAW converter and searched using the ProLuCID algorithm against a reverse-concatenated and nonredundant variant of the human UniProt database (2016-07). The precursor ion mass tolerance for a minimum envelop of three isotopic peaks was set to 50 ppm. Cysteine residues were searched with a static modification for carbamidomethylation (+57.02146 Da) and up to two differential modifications were allowed per peptide for methionine oxidation (+15.994915 Da). Lysine and N-termini residues were also searched with a static modification corresponding to the TMT tag (+229.1629 Da). Peptides were required to be a minimum of 6 amino acids long. ProLuCID data was filtered using DTAselect 2.0 within IP2 to allow for a false-positive rate less than 1% at the spectrum level. MS3-based peptide quantification was performed with a reporter ion mass tolerance set to 20 ppm with IP2. Proteins were required to have at least two unique peptides. Peptide-spectra matches were grouped based on protein ID and peptides were excluded if a) the sum of the reporter ion intensities was less than 10000, b) the coefficient of variance was greater than 0.5, or c) if they were non-unique or non-tryptic peptide sequences. Proteins were quantified by summing the reporter ion intensities across all matching peptide-spectra matches and normalizing to the highest signal channel per protein. Plots were generated with the $\log_2$ fold change of the quotient of DMSO treated cells with drug treated cells and the inverse $\log_{10}$ of a two-tailed Student's T-Test.

In vivo experiments

Studies were conducted in 6-8 week-old female NOD.Cg-PrkdcscidIl2rgtm1Wjl/SzJ (NSG) mice under the Institutional Animal Care and Use Committee (IACUC) protocol number 16-021 at Dana-Farber Cancer Institute. 1 x 10^6 MV4;11 cells were intravenously injected per mouse and engraftment was confirmed in the peripheral blood by flow cytometry-based detection of human CD45+ cells using an LSR Fortessa, BD Biosciences (human CD45-PE, clone HI30, 1:200, mouse CD45-APC-Cy7, clone 30-F11, 1:100, BioLegend). Upon confirmation of engraftment, mice were randomly assigned to treatment groups and received 3 doses of (*R*)-, (*S*)- dHTC1 (50

mg/kg i.p. BID, i.e. every 12 hours) or vehicle. The compounds were dissolved in 5% DMAC and 95% PEG-300 (40%) + NaCl (0.9%) (60%).

Mice were euthanized one hour after the last dosing using CO_2 inhalation followed by cervical dislocation. Bone marrow cells were isolated from tibias, femurs, iliac crest and spine by crushing the bones with mortar and pestle in PBS (Life Technologies) + 2% FBS (Life Technologies) and passing the cell suspension through a 40µM cell strainer (Falcon). Spleens were smashed using a syringe plunger and passed through a 40µM cell strainer (Falcon). Blood was collected by cardiac puncture and red blood cell lysis was performed using RBC lysis buffer (BioLegend). The differentiation status of bone marrow, spleen and blood cells was assessed by flow cytometry (LSR Fortessa, BD Biosciences) using the following antibodies: human CD45-PE, clone HI30, 1:200, mouse CD45-APC-Cy7, clone 30-F11, 1:100, and human CD11b-FITC, clone ICRF44, 1:100, BioLegend).

Ubiquitin Proteasome System Screen

Plasmids and oligonucleotides
The design and construction of the human UPS-focused sgRNA library used for ENL stability screens and the human CRBN deep mutational scanning (DMS) library have been described previously (*49, 70*). The engineering of the fluorescent protein stability reporter of ENL for the FACS-based CRISPR-Cas9 and DMS screens and the CRBN point mutants for the validation of the DMS screen were done as described previously (*29, 49*). The fluorescent protein stability reporter of GSPT1 was generated by inserting GSPT1 coding sequence into pArtichoke plasmid (Addgene 73320) by Gibson assembly.

FACS-based CRISPR-Cas9 ENL stability screen
The UPS-focused library packaged lentivirus containing supernatant was used to transduce KBM7 ENL-TagBFP-P2A-mCherry cells harboring a doxycycline-inducible Cas9 allele (iCas9) at a multiplicity of infection of 0.19 and 1,000x-fold library representation using 8µg/mL polybrene (Szabo Scandic, SACSC-134220). Library-transduced KBM7 cells were selected with 1mg/mL G418 (Gibco) for 14 days, expanded and Cas9 expression was induced with doxycycline at 0.4 µg/mL (PanReac AppliChem). Three days after doxycycline induction, 50 million cells per condition were treated with DMSO, dHTC1 (10µM) or SR-1114 (10µM) for 8h in two biological replicates. Cells were washed with PBS, stained with APC anti-mouse Thy1.1 antibody (1:400, 202526, BioLegend) and Zombie NIR Fixable Viability Dye (1:1000, BioLegend) in the presence of Human TruStain FcX Fc Receptor Blocking Solution (1:400, 422302, BioLegend) for 10min at 4°C in the dark, and fixed with 1mL BD CytoFix Fixation Buffer (BD Biosciences, 554655) for 30min at 4°C in the dark. Cells were washed with and stored in FACS buffer (PBS with 5% FCS and 1mM EDTA) at 4°C overnight. The next day, cells were strained through a 35µm nylon mesh and sorted on a BD FACSAria Fusion (BD Biosciences) iperated on BD FACSDiva software (v.8.0.2) using a 70µm nozzle excluding aggregates, dead (Zombie NIR positive), Cas9-negative (GFP negative) and sgRNA library-negative (Thy1.1-APC negative) cells. The remaining cells were sorted based on their ENL-BFP and mCherry levels into ENL^{hi} (5-10% of cells), ENL^{mid} (25-50%) and ENL^{low} (5-10%) fractions. Cells corresponding to at least 750-fold library representation were sorted per each sample replicate. DNA libraries of sorted fractions for Next-generation sequencing (NGS) were prepared as done previously (*88*). In short, genomic DNA was extracted by cell lysis (10mM Tris-HCl, 10mM EDTA, 150mM NaCl, 0.1% SDS), proteinase K treatment (New England Biolabs) and DNAse-free RNAse digest (Thermo Fisher), followed by two rounds of phenol extraction and isopropanol precipitation. Barcoded NGS libraries for each sorted fraction were prepared using a two-step PCR protocol using AmpliTaq Gold polymerase (Invitrogen). Barcodes for each sample were introduced in a first PCR, the product of which were purified using Mag-Bind TotalPure NGS beads (Omega Bio-tek) and amplified in a second PCR introducing the standard Illumina adapters. The final Illumina libraries were bead-purified, pooled and sequenced on NovaSeq 6000 instrument (Illumina) following a 100-base-pair, paired-end recipe. Screen analysis was performed as previously described (*88*). In short, sequencing reads were trimmed using fastx-toolkit (v0.0.14), aligned using Bowtie2 (v2.4.2) and quantified using featureCounts (v2.0.1). The crispr-process-nf Nextflow workflow is available at https://github.com/ZuberLab/crispr-process-nf/tree/566f6d46bbcc2a3f49f51bbc96b9820f408ec4a3. For statistical analysis, we used the crispr-mageck-nf Nextflow workflow, available at https://github.com/ZuberLab/crispr-mageck-nf/tree/c75a90f670698bfa78bfd8be786d6e5d6d4fc455. To calculate gene-level enrichment, the sorted populations (ENL^{high} or ENL^{low}) were compared to the ENL^{mid} populations in MAGeCK (0.5.9)(*89*), using median-normalized read counts.

FACS-based deep mutational scanning screens

18 million MV4;11 CRBN$^{-/-}$ ENL-TagBFP-P2A-mCherry cells were transduced with the CRBN DMS library virus supernatant at a multiplicity of infection of 0.17 yielding a calculated library representation of 1,760 cells per variant. For the transduction, 1 million cells were seeded in a 24-well plate with 8µg/mL polybrene (Szabo Scandic, SACSC-134220) and filled to 1mL with the titrated amount of virus and culture medium. The plate was centrifuged at 760g for 45min at 37°C and then cells were pooled and expanded. 3 days after transduction, library-transduced cells were selected with 1µg/mL Blasticidin (Gibco, R21001) for 7 days and selected cells were expanded. 50 million cells per condition were treated with dHTC1 (1µM) or SR-1114 (1µM) for 8h in three biological replicates. Cells were washed with PBS, stained with Zombie NIR Fixable Viability Dye (1:1000, BioLegend) for 10min at 4°C in the dark, and fixed with 1mL BD CytoFix Fixation Buffer (BD Biosciences, 554655) for 30min at 4°C in the dark. Cells were washed with and stored in FACS buffer (PBS with 5% FCS and 1mM EDTA) at 4°C overnight. Two sets of 50 million unsorted cells were also harvested as control, and directly washed and frozen. The next day, cells were strained through a 35µm nylon mesh and sorted on a BD FACSAria Fusion (BD Biosciences) operated on BD FACSDiva software (v.8.0.2) using a 70µm nozzle excluding aggregates, dead (Zombie NIR positive) and reporter negative (BFP and mCherry negative) cells. The remaining cells were sorted based on their ENL-BFP and mCherry levels into an ENL^{hi} fraction (30-35% of cells). Cells corresponding to at least 3,000-fold library representation were sorted per each sample replicate. DNA libraries of sorted and unsorted cell pools for Next-generation sequencing (NGS) were prepared as done previously (*49, 88*). In short, genomic DNA (gDNA) was extracted by cell lysis (10mM Tris-HCl, 10mM EDTA, 150mM NaCl, 0.1% SDS), proteinase K treatment (New England Biolabs) and DNAse-free RNAse digest (Thermo Fisher), followed by two rounds of phenol extraction and isopropanol precipitation. CRBN variant cDNAs were amplified via PCR from gDNA using AmpliTaq Gold polymerase (Invitrogen) and primers CRBN_GA_fwd (AGGTGTCGTGACGTACGGGATCCCAGGACCATGGCCGGCGAAGGAG) and CRBN_GA_rev (GGGGGGGGGGCGGAATTAATTCCTACTACTTACAAGCAAAGTATTACTTTGTCTGGAC). The cycle number for specific amplification of 1.4kb CRBN target was confirmed by agarose gel electrophoresis. PCR reactions for each sample were pooled and purified using Mag-Bind TotalPure NGS beads (Omega Bio-tek). The library preparation from the amplified DNA was performed using the Tagment DNA TDE1 Enzyme and IDT for Illumina Unique Dual Indexes (Illumina). Library concentrations were quantified with the Qubit 2.0 Fluorometric Quantitation system (Life Technologies) and the size distribution was assessed using the 2100 Bioanalyzer instrument (Agilent). For sequencing, samples were diluted and pooled into NGS libraries and sequenced on NovaSeq 6000 instrument (Illumina) following a 100-base-pair, paired-end recipe. Raw sequencing reads were converted to fastq format with samtools (v1.15.1) and bedtools (v.2.30.0) using bamtofastq function. Sequencing reads were trimmed using Trim Galore (v0.6.6) using nextera and pair modes. Short reads were aligned to the CRBN cassette and SAM files were generated using mem algorithm from the bwa software package (v0.7.17). SAM file was converted to BAM using samtools and mutation calling was performed using the AnalyzeSaturationMutagenesis tool from GATK (v4.1.8.1). Given our sequencing strategy, >98% of reads corresponded to wild-type sequences and were filtered out during this step. Next, relative frequencies of variants were calculated for each position and variants that were covered by less than 1 in 30,000 reads were excluded from further analysis. Read counts for each variant were then normalized to total read count of each sample and $\log_2$ fold changes of ENL^{high} over unsorted pools were calculated. To correct for differential drug potency, each variant was then normalized to the maximum $\log_2$ fold change. For drug comparisons, $\log_2$ fold changes of ENL^{high} over unsorted pools of each drug were subtracted. Heatmaps were generated using pheatmap (v.1.0.12) package in R (v.4.1.0) or with Prism version 10.

Flow-cytometric ENL reporter assay

MV4;11 CRBN$^{-/-}$ ENL-TagBFP-P2A-mCherry or GSPT1-GFP-P2A-mCherry cells were transduced with lentivirus expressing wild-type or mutated CRBN in pRRL-EF1a-CRBN-IRES-BlastR plasmid to generate stable cell lines. For evaluation of reporter degradation on the different CRBN backgrounds, cells were treated with DMSO or dHTC1, SR-1114 (both 1µM, 6h, ENL reporter) or CC885 (1µM, 5h, GSPT1 reporter) before flow cytometry analysis on an LSR Fortessa (BD Biosciences) operated on BD FACSDiva software (v9.0).

Crystallization of CRBN^{midi} bound to dHTC1

CRBN^{midi} at 3.4 mg/mL in a buffer containing 20 mM HEPES pH 7.5, 500 mM NaCl and 0.5 mM TCEP was mixed with a 4-molar excess of dHTC1 (364 µM, 1.8% (v/v) DMSO final). The complex was subjected to co-crystallization using the sitting drop vapor diffusion method across several sparse matrix screens at 20°C by mixing equal volumes of protein solution and reservoir solution. Crystal hits from Morpheus H10 (0.1 M Buffer System 3 pH 8.5, 0.12 M Alcohols, 30 % Precipitant Mix 2) (Molecular Dimensions) were harvested directly from the drop and flash cooled in liquid nitrogen.

Diffraction data were collected at Diamond Light Source beamline I24 using the Eiger CdTe 9M detector at a wavelength of 0.6199 Å. The 2.2 Å dataset was processed using Dials (*90*), indexed in $P3_1$ space group and the structure was solved by molecular replacement in phenix.phaser (*91*) using the coordinates of 8RQA as a search model. Phenix.refine (*92*) and coot (*93*) were used for refinement and model building.

Surface plasmon resonance

Surface plasmon resonance experiments were performed on a Biacore S200 (Cytiva). A series S streptavidin sensor chip was used for ligand immobilization (Cytiva). Biotinylated ENL and biotinylated CRBN^{midi} were prepared in HBS-EP+ buffer (10 mM HEPES, 150 mM NaCl, 3 mM EDTA, 0.05% P20, pH 7.4) or PBS-P+ (Cytiva). Ligand immobilization was carried out in flow cell 2 and 4 with a series of ligand injections at a flow rate of 5 mL/min, until the desired density was achieved (700 RU for ENL, and 4432 RU for CRBN^{midi}). Flow cells 1 and 3 were left blank as a reference. HBS-EP+ buffer with 1% DMSO was used as running buffer and for the preparation of all analyte samples. For samples with CRBN-DDB1 in the eluent, CRBN-DDB1 was serially diluted in either HBS-EP+ and 1% DMSO buffer or HBS-EP+ and 1% DMSO buffer with 1 µM compound. Analytes were serially diluted in polystyrene 96 well plates immediately prior to injection. Before analyte injection, 3 startup cycles were run with injections of running buffer over all flow cells. Binding data was collected by injecting the analyte at a flow rate of 30 mL/min over two flow cells (reference and immobilized ligand) at a temperature of 25 °C. The association to biotin-ENL or CRBN^{midi} was measured over 60 seconds, and the dissociation over 180 seconds. The flow cell surfaces were regenerated with 30 second injections of running buffer over each flow cell. Duplicate injections were carried out for each sample, including the blank. Affinity curves, association and dissociation constants, and sensograms were determined using Biacore S200 evaluation software.

RNA sequencing

Total RNA was extracted from mouse cell-depleted bone marrow cells from MV4;11 xenografts using the RNeasy Kit (Qiagen). RNA samples were run on a tape station (Agilent) to assure an RNA integrity (RIN) score > 8, and quantified by Qbit (Thermo Fisher). The NEBNext Poly(A) mRNA Magnetic Isolation Module and NEBNext Ultra II RNA Library Prep Kit (NEB BioLabs) were used to prepare RNA libraries. Sequencing was performed using the NextSeq500 (Illumina) as 37-bp paired-end sequencing with 20 million reads. Further analysis was performed on expressed genes (rlog expression < 3).

Cryogenic electron microscopy

Cloning, protein expression and purification
His_6-tagged hsDDB1$^{\Delta BPB}$ (UniProt: Q16531, aa396–705 replaced with a GNGNSG linker) and FLAG-tagged hsCRBN (UniProt: Q96SW2) were cloned into pAC8-derived vectors (*94*) and recombinantly expressed using the baculovirus expression system (Invitrogen). To generate baculovirus, 1 µg of pAC8-derived plasmids were co-transfected with linearized baculoviral DNA in *Spodoptera frugiperda* Sf9 cells grown in ESF 921 medium (Expression Systems) at a density of 1.0×10^6 cells/ml. Viral titer was increased by three rounds of amplification in Sf9 cells. For protein expression, *Trichoplusia ni* High Five cells grown in SF-4 Baculo Express ICM (BioConcept) at a density of 2×10^6 cells/ml were coinfected with 1.5% (v/v) each of DDB1$^{\Delta BPB}$ - and CRBN-expressing baculoviruses. After 48 hours of incubation, cells were collected (20 min, 3,300 *g*). Cells were resuspended and sonicated in lysis buffer [50 mM HEPES/NaOH, pH 7.4, 200 mM NaCl, 0.1% (v/v) Triton X-100, 1 mM TCEP] supplemented with protease inhibitors. The cell lysate was treated with Benzonase for 10 min and cleared by ultracentrifugation (60 min, 120,000 *g*), the supernatant was incubated with FLAG-antibody-coated beads (Genscript, L00432) and washed with wash buffer (50 mM HEPES/NaOH, pH 8.0, 200 mM NaCl).

Bound proteins were eluted with 0.15 mg/ml 1×FLAG (DYKDDDK) peptide and diluted to 50 mM NaCl with IEX buffer A (50 mM HEPES/NaOH, pH 7.4, 1 mM TCEP). Samples were added to Poros 50 HQ resin (Thermo Scientific) and eluted with a linear salt gradient from 50 mM to 1000 mM. Peak fractions from anion-exchange chromatography were concentrated using centrifugal concentrators (Amicon, 30kDa molecular weight cut-off (MWCO)) and polished by size exclusion chromatography (SEC, HiLoad 16/600 Supderdex 200 pg, Cytiva) in SEC buffer (50 mM HEPES/NaOH pH 7.4, 150 mM NaCl, 1 mM TCEP). Peak fractions were concentrated by centrifugation, flash frozen in liquid nitrogen, and stored at -80 ºC.

His_6-tagged ENL YEATS domain (aa1-148, UniProt: Q03111) was cloned into a pNIC-Bio2 (SGC Oxford) vector and expressed in a LOBSTR *E.coli* expression strain (Kerafast, EC1002). After transformation, 2 L cultures in TB medium were grown at 37 ºC to an OD_{600} of ~0.6 and induced with 0.35 mM Isopropyl ß-D-1-thiogalactopyranoside (IPTG). Temperature was decreased to 18 ºC, proteins were expressed overnight, and cultures were harvested by centrifugation (20 min, 3,300 *g*). Cell pellets were resuspended in lysis buffer [50 mM HEPES/NaOH pH 7.4, 200 mM NaCl, 20 mM imidazole, 5% (v/v) glycerol, 1mM TCEP] supplemented with protease inhibitors and lysed using sonication. After clearance by ultracentrifugation (60 min, 120,000 *g*), the supernatant was treated with Benzonase for 10 min and incubated with high affinity Ni-charged resin (Genscript, L00223) and eluted with increasing imidazole concentrations (150 – 750 mM). Elution fractions were concentrated using a 10 kDa MWCO centrifugal concentrator and polished by SEC (Superdex 75 Increase 10/300 GL, Cytiva) in SEC buffer (30 mM HEPES/NaOH pH 7.4, 300 mM NaCl, 3 mM TCEP). Peak fractions were concentrated by centrifugation, flash frozen in liquid nitrogen, and stored at -80 °C.

EM sample preparation and data collection

$DDB1^{\Delta BPB}$•CRBN, dHTC1, and ENL YEATS were mixed and incubated on ice for 1 hour at final concentration of 1.4, 14, 2.8 µM (dataset1) and 1.6, 16, 3.2 µM (dataset 2) respectively, keeping DMSO concentrations below 2% (v/v). Grids (Quantifoil UltrAuFoil R 0.6/1) were glow-discharged (20 mA, 120 s, 39 Pa) and vitrified in a Leica EM-GP operated at 10°C and 90% relative humidity. Grids were preincubated with 4 µl of 10 µM CRBN agnostic IKZF1 (aa140-196, Q146A; G151N) for 1 min and then blotted from behind for 4 s with NCI Micro Whatman No.1 filter paper. Immediately, 4 µl of the sample were applied to the grids before blotting for 4 s and plunging into liquid ethane, kept at −181 °C. Datasets were collected using Smart EPU (v3.7) n a Thermo Scientific Titan Krios equipped with a Thermo Fisher Scientific Selectris energy filter (10 eV slit width) and Thermo Fisher Scientific Falcon 4 direct electron detector. Movies (49 frames per movie, 2.87 s exposure time) were acquired at 300 kV at a nominal magnification of 165,000× in counting mode with a pixel size of 0.736 Å/pixel. One movie was recorded per hole with aberration-free image shift (as implemented in EPU). 9,856 movies for dataset 1 and 13,027 movies for dataset 2 were recorded with defocus varying from -0.8 to -2.0 µm and a total exposure rate of 50.22 e^-/A^2.

Data processing and model building

CryoSPARC (v4.5.3) was used for all processing steps (*95*). All resolutions given are based on the Fourier shell correlation (FSC) 0.143 threshold criterion. For dataset 1, 9,856 movies were corrected for beam-induced motion and contrast transfer function (CTF) was estimated on-the-fly in cryoSPARC live. Low-quality movies were rejected, and 1,267,417 particles were extracted (1.31 Å/pixel) from the 6,558 remaining micrographs after TOPAZ (v0.2.5a) particle picking. The particles were cleaned up in three rounds of heterogeneous refinement. Preferred orientation became apparent at this step. Thus, the remaining 994,856 particles were further classified using heterogeneous refinement, which revealed a small number of classes (95,520 particles) representing a more balanced range of views. The selected 95,520 particles were re-extracted at 0.92 Å/pixel. For dataset 2, 13,027 movies were corrected from beam-induced motion and contrast transfer function (CTF) was estimated on-the-fly in cryoSPARC live. Low-quality movies were rejected, and the remaining 11,541 micrographs were split into two groups, resulting in 5,173,911 particles extracted (1.31 Å/pixel) after TOPAZ (v0.2.5a) particle picking. The particles were cleaned up in two rounds of heterogeneous refinement. Similarly to data set 1, the resulting 1,536,327 particles were further classified using heterogeneous refinement, which again revealed a small number of classes (89,792 particles) with more balanced views. The selected 89,792 particles were re-extracted at 0.92 Å/pixel and pooled with the particles from dataset 1. The pooled particles were used in a final homogeneous refinement, yielding a consensus reconstruction at global resolution of 2.6 Å with a B factor of 84.8 $Å^2$ (EMD-XXXX). Local refinement with a soft mask encompassing CRBN and ENL YEATS yielded a final reconstruction at 2.9 Å (EMD-XXXX), which was followed by postprocessing using deepEMhancer to improve

the density for ENL YEATS. Maps obtained after homogeneous refinement, local refinement focused on the CRBN/ENL YEATS mask, postprocessing using deepEMhancer were used for model building. CRBN [PDB ID 8TNQ] and ENL YEATS [PDB ID 6HPY] were fit into the density in UCSF ChimeraX (v1.6.1) (*96*) and relaxed using ISOLDE (v1.6.0) (*97*) and Rosetta (v3.13) (*98*). The relaxed model was manually adjusted in COOT (v0.9.8.0) (*93*) and prepared for refinement with phenix.ready_set (v1.19.2-4158) (*99*), followed by refinement using ligand restraints in phenix.real_space_refine (v1.19.2-4158) (*92*) against the unsharpened maps. DDB1$^{\Delta BPB}$ [PDB ID 8TNQ] was individually fit into the map obtained after homogeneous refinement using UCSF ChimeraX (v1.6.1) (*96*) and manually adjusted in COOT. The combined DDB1$^{\Delta BPB}$•CRBN/dHTC1/ENL YEATS model went through phenix.real_space_refine and manually adjusted in COOT prior to final refinement in phenix.real_space_refine. The final model and map were deposited in PDB as XXXX and EMDB as XXXXX. Structural biology applications used in this project were compiled and configured by SBGrid (*100*).

Interface analysis

Interface comparison was made with Rosetta (v3.13) by reordering the jump number of fold tree so that CRBN and ENL YEATS interface should be compared, and then used the following command to obtain buried interface solvent-accessible surface area and shape complementarity score (*52*): sasa_and_sc_calc_scripts.sh

References

1. S. L. Schreiber, The Rise of Molecular Glues. *Cell* **184**, 3-9 (2021).
2. B. Z. Stanton, E. J. Chory, G. R. Crabtree, Chemically induced proximity in biology and medicine. *Science* **359**, (2018).
3. S. L. Schreiber, G. R. Crabtree, The mechanism of action of cyclosporin A and FK506. *Immunol Today* **13**, 136-142 (1992).
4. E. J. Brown *et al.*, A mammalian protein targeted by G1-arresting rapamycin-receptor complex. *Nature* **369**, 756-758 (1994).
5. D. A. Nalawansha, K. Mangano, W. den Besten, P. R. Potts, TAC-tics for Leveraging Proximity Biology in Drug Discovery. *Chembiochem* **25**, e202300712 (2024).
6. G. M. Burslem, C. M. Crews, Proteolysis-Targeting Chimeras as Therapeutics and Tools for Biological Discovery. *Cell* **181**, 102-114 (2020).
7. Z. Kozicka, N. H. Thomä, Haven't got a glue: Protein surface variation for the design of molecular glue degraders. *Cell Chem Biol* **28**, 1032-1047 (2021).
8. T. Ito *et al.*, Identification of a primary target of thalidomide teratogenicity. *Science* **327**, 1345-1350 (2010).
9. A. Lopez-Girona *et al.*, Cereblon is a direct protein target for immunomodulatory and antiproliferative activities of lenalidomide and pomalidomide. *Leukemia* **26**, 2326-2335 (2012).
10. J. Krönke *et al.*, Lenalidomide causes selective degradation of IKZF1 and IKZF3 in multiple myeloma cells. *Science* **343**, 301-305 (2014).
11. G. Lu *et al.*, The myeloma drug lenalidomide promotes the cereblon-dependent destruction of Ikaros proteins. *Science* **343**, 305-309 (2014).
12. J. Krönke *et al.*, Lenalidomide induces ubiquitination and degradation of CK1α in del(5q) MDS. *Nature* **523**, 183-188 (2015).
13. M. E. Matyskiela *et al.*, A novel cereblon modulator recruits GSPT1 to the CRL4(CRBN) ubiquitin ligase. *Nature* **535**, 252-257 (2016).
14. G. Petzold, E. S. Fischer, N. H. Thomä, Structural basis of lenalidomide-induced CK1α degradation by the CRL4(CRBN) ubiquitin ligase. *Nature* **532**, 127-130 (2016).
15. E. R. Watson *et al.*, Molecular glue CELMoD compounds are regulators of cereblon conformation. *Science* **378**, 549-553 (2022).
16. K. A. Donovan *et al.*, Thalidomide promotes degradation of SALL4, a transcription factor implicated in Duane Radial Ray syndrome. *Elife* **7**, (2018).
17. M. E. Matyskiela *et al.*, Crystal structure of the SALL4-pomalidomide-cereblon-DDB1 complex. *Nat Struct Mol Biol* **27**, 319-322 (2020).
18. N. Kerres *et al.*, Chemically Induced Degradation of the Oncogenic Transcription Factor BCL6. *Cell Rep* **20**, 2860-2875 (2017).
19. M. Słabicki *et al.*, Small-molecule-induced polymerization triggers degradation of BCL6. *Nature* **588**, 164-168 (2020).
20. M. Słabicki *et al.*, The CDK inhibitor CR8 acts as a molecular glue degrader that depletes cyclin K. *Nature* **585**, 293-297 (2020).
21. C. Mayor-Ruiz *et al.*, Rational discovery of molecular glue degraders via scalable chemical profiling. *Nat Chem Biol* **16**, 1199-1207 (2020).
22. L. Lv *et al.*, Discovery of a molecular glue promoting CDK12-DDB1 interaction to trigger cyclin K degradation. *Elife* **9**, (2020).
23. M. Lim *et al.*, DCAF16-Based Covalent Handle for the Rational Design of Monovalent Degraders. *ACS Central Science*, (2024).
24. E. S. Toriki *et al.*, Rational Chemical Design of Molecular Glue Degraders. *ACS Cent Sci* **9**, 915-926 (2023).
25. Y. D. Li *et al.*, Template-assisted covalent modification underlies activity of covalent molecular glues. *Nat Chem Biol*, (2024).
26. P. Filippakopoulos *et al.*, Selective inhibition of BET bromodomains. *Nature* **468**, 1067-1073 (2010).
27. M. Lim *et al.*, DCAF16-Based Covalent Handle for the Rational Design of Monovalent Degraders. *ACS Cent Sci* **10**, 1318-1331 (2024).
28. A. G. Shergalis *et al.*, CRISPR Screen Reveals BRD2/4 Molecular Glue-like Degrader via Recruitment of DCAF16. *ACS Chem Biol* **18**, 331-339 (2023).

29. O. Hsia *et al.*, Targeted protein degradation via intramolecular bivalent glues. *Nature* **627**, 204-211 (2024).
30. G. S. Parker *et al.*, Discovery of Monovalent Direct Degraders of BRD4 That Act Via the Recruitment of DCAF11. *Mol Cancer Ther*, (2024).
31. S. Li, P. Wu, J. E. Moses, K. B. Sharpless, Multidimensional SuFEx Click Chemistry: Sequential Sulfur(VI) Fluoride Exchange Connections of Diverse Modules Launched From An SOF4 Hub. *Angewandte Chemie International Edition* **56**, 2903-2908 (2017).
32. S. Kitamura *et al.*, Sulfur(VI) Fluoride Exchange (SuFEx)-Enabled High-Throughput Medicinal Chemistry. *J Am Chem Soc* **142**, 10899-10904 (2020).
33. F. Liu *et al.*, Biocompatible SuFEx Click Chemistry: Thionyl Tetrafluoride (SOF(4))-Derived Connective Hubs for Bioconjugation to DNA and Proteins. *Angew Chem Int Ed Engl* **58**, 8029-8033 (2019).
34. T. R. Carter *et al.*, SuFEx-based chemical diversification for the systematic discovery of CRBN molecular glues. *Bioorg Med Chem* **104**, 117699 (2024).
35. L. Garnar-Wortzel *et al.*, Chemical Inhibition of ENL/AF9 YEATS Domains in Acute Leukemia. *ACS Cent Sci* **7**, 815-830 (2021).
36. W.-J. He *et al.*, Pd(COD)(DQ): A Stable, Versatile, and Monometallic Palladium(0) Source for Organometallic Synthesis and Catalysis. *ChemRxiv*, (2024).
37. A. Zogu *et al.*, Perfluorooxosulfate Salts as SOF(4)-Gas-Free Precursors to Multidimensional SuFEx Electrophiles. *Angew Chem Int Ed Engl* **63**, e202403797 (2024).
38. M. A. Erb *et al.*, Transcription control by the ENL YEATS domain in acute leukaemia. *Nature* **543**, 270-274 (2017).
39. L. Wan *et al.*, ENL links histone acetylation to oncogenic gene expression in acute myeloid leukaemia. *Nature* **543**, 265-269 (2017).
40. G. Tin *et al.*, Discovery of a DCAF11-dependent cyanoacrylamide-containing covalent degrader of BET-proteins. *Bioorg Med Chem Lett* **107**, 129779 (2024).
41. G. Xue *et al.*, Discovery of a Drug-like, Natural Product-Inspired DCAF11 Ligand Chemotype. *Nature Communications* **14**, 7908 (2023).
42. C. Mayor-Ruiz *et al.*, Plasticity of the Cullin-RING Ligase Repertoire Shapes Sensitivity to Ligand-Induced Protein Degradation. *Mol Cell* **75**, 849-858.e848 (2019).
43. S. Ichikawa *et al.*, The E3 ligase adapter cereblon targets the C-terminal cyclic imide degron. *Nature* **610**, 775-782 (2022).
44. C. Heim, A.-K. Spring, S. Kirchgäßner, D. Schwarzer, M. D. Hartmann, Identification and structural basis of C-terminal cyclic imides as natural degrons for cereblon. *Biochemical and Biophysical Research Communications* **637**, 66-72 (2022).
45. T. Ito, Y. Yamaguchi, H. Handa, Exploiting ubiquitin ligase cereblon as a target for small-molecule compounds in medicine and chemical biology. *Cell Chem Biol* **28**, 987-999 (2021).
46. G. E. Winter *et al.*, BET Bromodomain Proteins Function as Master Transcription Elongation Factors Independent of CDK9 Recruitment. *Mol Cell* **67**, 5-18.e19 (2017).
47. A. Kroupova *et al.*, Design of a Cereblon construct for crystallographic and biophysical studies of protein degraders. *bioRxiv*, 2024.2001.2017.575503 (2024).
48. M. S. Gadd *et al.*, Structural basis of PROTAC cooperative recognition for selective protein degradation. *Nat. Chem. Biol.* **13**, 514 (2017).
49. A. Hanzl *et al.*, Functional E3 ligase hotspots and resistance mechanisms to small-molecule degraders. *Nat Chem Biol* **19**, 323-333 (2023).
50. T. D. Goddard *et al.*, UCSF ChimeraX: Meeting modern challenges in visualization and analysis. *Protein Sci* **27**, 14-25 (2018).
51. E. S. Fischer *et al.*, Structure of the DDB1-CRBN E3 ubiquitin ligase in complex with thalidomide. *Nature* **512**, 49-53 (2014).
52. M. C. Lawrence, P. M. Colman, Shape complementarity at protein/protein interfaces. *J Mol Biol* **234**, 946-950 (1993).
53. J. A. M. Mercer *et al.*, Continuous evolution of compact protein degradation tags regulated by selective molecular glues. *Science* **383**, eadk4422 (2024).
54. Z. Kozicka *et al.*, Design principles for cyclin K molecular glue degraders. *Nat Chem Biol* **20**, 93-102 (2024).
55. Y. D. Li *et al.*, Template-assisted covalent modification of DCAF16 underlies activity of BRD4 molecular glue degraders. *bioRxiv*, (2023).

56. M. Mondal, A. K. H. Hirsch, Dynamic combinatorial chemistry: a tool to facilitate the identification of inhibitors for protein targets. *Chemical Society Reviews* **44**, 2455-2488 (2015).
57. K.-N. Yan *et al.*, Accelerating PROTACs Discovery Through a Direct-to-Biology Platform Enabled by Modular Photoclick Chemistry. *Advanced Science* **11**, 2400594 (2024).
58. R. Stevens *et al.*, Integrated Direct-to-Biology Platform for the Nanoscale Synthesis and Biological Evaluation of PROTACs. *Journal of Medicinal Chemistry* **66**, 15437-15452 (2023).
59. R. P. Thomas *et al.*, A direct-to-biology high-throughput chemistry approach to reactive fragment screening. *Chem. Sci.* **12**, 12098 (2021).
60. C. E. Hendrick *et al.*, Direct-to-Biology Accelerates PROTAC Synthesis and the Evaluation of Linker Effects on Permeability and Degradation. *ACS Medicinal Chemistry Letters* **13**, 1182-1190 (2022).
61. J. W. Mason *et al.*, DNA-encoded library-enabled discovery of proximity-inducing small molecules. *Nat Chem Biol* **20**, 170-179 (2024).
62. S. Liu *et al.*, Rational Screening for Cooperativity in Small-Molecule Inducers of Protein-Protein Associations. *J Am Chem Soc* **145**, 23281-23291 (2023).
63. J. Poirson *et al.*, Proteome-scale discovery of protein degradation and stabilization effectors. *Nature* **628**, 878-886 (2024).
64. Y. V. Serebrenik, D. Mani, T. Maujean, G. M. Burslem, O. Shalem, Pooled endogenous protein tagging and recruitment for scalable discovery of effectors for induced proximity therapeutics. *bioRxiv*, (2023).
65. X. Zhang, V. M. Crowley, T. G. Wucherpfennig, M. M. Dix, B. F. Cravatt, Electrophilic PROTACs that degrade nuclear proteins by engaging DCAF16. *Nat Chem Biol* **15**, 737-746 (2019).
66. X. Zhang *et al.*, DCAF11 Supports Targeted Protein Degradation by Electrophilic Proteolysis-Targeting Chimeras. *J Am Chem Soc* **143**, 5141-5149 (2021).
67. R. C. Sarott *et al.*, Chemical Specification of E3 Ubiquitin Ligase Engagement by Cysteine-Reactive Chemistry. *J Am Chem Soc* **145**, 21937-21944 (2023).
68. D. Y. Nie *et al.*, Recruitment of FBXO22 for targeted degradation of NSD2. *Nat Chem Biol*, (2024).
69. A. A. Basu *et al.*, A CRISPR activation screen identifies FBXO22 supporting targeted protein degradation. *Nat Chem Biol*, (2024).
70. C. Kagiou *et al.*, Alkylamine-tethered molecules recruit FBXO22 for targeted protein degradation. *Nat Commun* **15**, 5409 (2024).
71. C. E. Powell *et al.*, Selective Degradation of GSPT1 by Cereblon Modulators Identified via a Focused Combinatorial Library. *ACS Chemical Biology* **15**, 2722-2730 (2020).
72. G. Nishiguchi *et al.*, Identification of Potent, Selective, and Orally Bioavailable Small-Molecule GSPT1/2 Degraders from a Focused Library of Cereblon Modulators. *J Med Chem* **64**, 7296-7311 (2021).
73. E. S. Wang *et al.*, Acute pharmacological degradation of Helios destabilizes regulatory T cells. *Nat Chem Biol* **17**, 711-717 (2021).
74. A. L. Verano *et al.*, Redirecting the Neo-Substrate Specificity of Cereblon-Targeting PROTACs to Helios. *ACS Chem Biol* **17**, 2404-2410 (2022).
75. S. Bonazzi *et al.*, Discovery and characterization of a selective IKZF2 glue degrader for cancer immunotherapy. *Cell Chem Biol* **30**, 235-247.e212 (2023).
76. A. Ng *et al.*, Discovery of Molecular Glue Degraders via Isogenic Morphological Profiling. *ACS Chemical Biology* **18**, 2464-2473 (2023).
77. Z. Wang *et al.*, Direct-to-biology, automated, nano-scale synthesis, and phenotypic screening-enabled E3 ligase modulator discovery. *Nature Communications* **14**, 8437 (2023).
78. P. Y. Ting *et al.*, A molecular glue degrader of the WIZ transcription factor for fetal hemoglobin induction. *Science* **385**, 91-99 (2024).
79. M. Ishoey *et al.*, Translation Termination Factor GSPT1 Is a Phenotypically Relevant Off-Target of Heterobifunctional Phthalimide Degraders. *ACS Chem Biol* **13**, 553-560 (2018).
80. M. E. Matyskiela *et al.*, SALL4 mediates teratogenicity as a thalidomide-dependent cereblon substrate. *Nat Chem Biol* **14**, 981-987 (2018).
81. T. M. Nguyen *et al.*, Proteolysis-targeting chimeras with reduced off-targets. *Nat Chem* **16**, 218-228 (2024).
82. B. Knoche, G. Blaschke, Investigations on the in vitro racemization of thalidomide by high-performance liquid chromatography. *Journal of Chromatography A* **666**, 235-240 (1994).
83. J. N. Asiaban *et al.*, Cell-Based Ligand Discovery for the ENL YEATS Domain. *ACS Chem Biol* **15**, 895-903 (2020).

84. Y. Perez-Riverol *et al.*, The PRIDE database resources in 2022: a hub for mass spectrometry-based proteomics evidences. *Nucleic Acids Res* **50**, D543-d552 (2022).
85. M. R. Lazear *et al.*, Proteomic discovery of chemical probes that perturb protein complexes in human cells. *Mol Cell* **83**, 1725-1742.e1712 (2023).
86. E. V. Vinogradova *et al.*, An Activity-Guided Map of Electrophile-Cysteine Interactions in Primary Human T Cells. *Cell* **182**, 1009-1026.e1029 (2020).
87. L. Ting, R. Rad, S. P. Gygi, W. Haas, MS3 eliminates ratio distortion in isobaric multiplexed quantitative proteomics. *Nat Methods* **8**, 937-940 (2011).
88. M. de Almeida *et al.*, AKIRIN2 controls the nuclear import of proteasomes in vertebrates. *Nature* **599**, 491-496 (2021).
89. W. Li *et al.*, MAGeCK enables robust identification of essential genes from genome-scale CRISPR/Cas9 knockout screens. *Genome Biol* **15**, 554 (2014).
90. G. Winter *et al.*, DIALS: implementation and evaluation of a new integration package. *Acta Crystallogr D Struct Biol* **74**, 85-97 (2018).
91. A. J. McCoy *et al.*, Phaser crystallographic software. *J Appl Crystallogr* **40**, 658-674 (2007).
92. P. V. Afonine *et al.*, Towards automated crystallographic structure refinement with phenix.refine. *Acta Crystallogr D Biol Crystallogr* **68**, 352-367 (2012).
93. P. Emsley, B. Lohkamp, W. G. Scott, K. Cowtan, Features and development of Coot. *Acta Crystallogr D Biol Crystallogr* **66**, 486-501 (2010).
94. W. Abdulrahman *et al.*, A set of baculovirus transfer vectors for screening of affinity tags and parallel expression strategies. *Anal Biochem* **385**, 383-385 (2009).
95. A. Punjani, J. L. Rubinstein, D. J. Fleet, M. A. Brubaker, cryoSPARC: algorithms for rapid unsupervised cryo-EM structure determination. *Nat Methods* **14**, 290-296 (2017).
96. E. F. Pettersen *et al.*, UCSF ChimeraX: Structure visualization for researchers, educators, and developers. *Protein Sci* **30**, 70-82 (2021).
97. T. I. Croll, ISOLDE: a physically realistic environment for model building into low-resolution electron-density maps. *Acta Crystallogr D Struct Biol* **74**, 519-530 (2018).
98. J. K. Leman *et al.*, Macromolecular modeling and design in Rosetta: recent methods and frameworks. *Nat Methods* **17**, 665-680 (2020).
99. P. D. Adams *et al.*, PHENIX: a comprehensive Python-based system for macromolecular structure solution. *Acta Crystallogr D Biol Crystallogr* **66**, 213-221 (2010).
100. A. Morin *et al.*, Collaboration gets the most out of software. *Elife* **2**, e01456 (2013).